JGR Space Physics

RESEARCH ARTICLE
10.1029/2023JA032201

Key Points:

- The correlation between the electron density and temperature in the topside ionosphere has been investigated through 9 years of Swarm B in-situ observations
- The latitudinal, diurnal, and seasonal variations of the correlation have been studied on a global scale at an unprecedented spatial and temporal resolution
- First ever study of the correlation at high latitudes, which highlighted a general pattern of negative correlation except for the summer season at the polar cusp

Correspondence to:
A. Pignalberi,
alessio.pignalberi@ingv.it

Citation:
Pignalberi, A., Giannattasio, F., Truhlik, V., Coco, I., Pezzopane, M., & Alberti, T. (2024). Investigating the main features of the correlation between electron density and temperature in the topside ionosphere through Swarm satellites data. *Journal of Geophysical Research: Space Physics*, *129*, e2023JA032201. https://doi.org/10.1029/2023JA032201

Received 20 OCT 2023
Accepted 29 FEB 2024

Author Contributions:
Conceptualization: A. Pignalberi, F. Giannattasio
Data curation: A. Pignalberi, V. Truhlik, I. Coco
Formal analysis: A. Pignalberi
Investigation: A. Pignalberi, F. Giannattasio, V. Truhlik, M. Pezzopane, T. Alberti
Methodology: A. Pignalberi, F. Giannattasio, I. Coco
Software: A. Pignalberi
Supervision: M. Pezzopane
Validation: A. Pignalberi, V. Truhlik
Visualization: A. Pignalberi
Writing – original draft: A. Pignalberi, F. Giannattasio, V. Truhlik, I. Coco, T. Alberti
Writing – review & editing: A. Pignalberi, F. Giannattasio, V. Truhlik, I. Coco, M. Pezzopane, T. Alberti

Investigating the Main Features of the Correlation Between Electron Density and Temperature in the Topside Ionosphere Through Swarm Satellites Data

A. Pignalberi[1], F. Giannattasio[1], V. Truhlik[2], I. Coco[1], M. Pezzopane[1], and T. Alberti[1]

[1]Istituto Nazionale di Geofisica e Vulcanologia, Roma, Italy, [2]Institute of Atmospheric Physics of the Czech Academy of Sciences, Prague, Czech Republic

Abstract Electron density (N_e) and electron temperature (T_e) observations collected by Langmuir Probes on board the European Space Agency (ESA) Swarm B satellite are used to characterize their correlation in the topside ionosphere at an altitude of about 500 km. Spearman correlation coefficient values ($R_{Spearman}$) are calculated on joint probability distributions between N_e and T_e for selected conditions. The large data set of Swarm B observations at 2-Hz rate, covering the years 2014–2022, allowed investigating the correlation properties of the topside ionospheric plasma on a global scale, for different diurnal and seasonal conditions, with both a coverage and a detail never reached before. Results are given as maps of $R_{Spearman}$ as a function of the Quasi-Dipole (QD) magnetic latitude and magnetic local time (MLT) coordinates. The characterization of the correlation at high latitudes, along with the description of the diurnal trend at all latitudes, are the new findings of this study. The main correlation features point out a negative correlation at the morning overshoot, during daytime at mid latitudes, and during nighttime at the ionospheric trough and subauroral latitudes. Conversely, a positive correlation dominates the nighttime hours at mid and low latitudes and, to a minor extent, the low latitudes from 09 MLT onwards. A seasonal dependence of the correlation is noticeable only at very high latitudes where the general pattern of the negative correlation does not hold around ±75° QD latitude in the summer season. Results from Swarm B have been statistically compared and discussed with observations from the Arecibo, Jicamarca, and Millstone Hill incoherent scatter radars.

1. Introduction

The first simultaneous observations of electron density (N_e) and electron temperature (T_e) in the ionosphere date back to 60s and 70s thanks to the development of ground-based facilities as incoherent scatter radars (ISRs), and satellite-based instruments as Langmuir Probes (LPs) and Retarding Potential Analyzers (RPAs) (Hunsucker, 1991). The first observations evidenced a so well-established anti-correlation (i.e., negative correlation) between N_e and T_e on which the first empirical models of ionospheric T_e relied on (Bilitza, 1975, 1983; Brace & Theis, 1978; Mahajan, 1977; McDonald & Williams, 1980; Taylor & Risk, 1974). At that time, the opportunity to retrieve T_e from N_e was very attractive since N_e observations, compared to T_e, were more easily accessible through ionosondes in the bottomside ionosphere, topside sounders in the topside ionosphere, and ISRs in both bottomside and topside ionosphere. Indeed, in the 60s and 70s the knowledge of the horizontal distribution of N_e at the F2-layer peak (the absolute maximum of N_e in the ionosphere), on a global scale, was already well-established through the works of Jones and Gallet (1962, 1965), and the corresponding vertical profile modeled through the first implementations of the International Reference Ionosphere (IRI) model (Bilitza et al. (2022) and references therein). This is why early representations of T_e in the IRI model relied on its anti-correlation with N_e (Bilitza, 1975, 1983). However, at that time most of the investigations were based on data sets biased toward conditions where the anti-correlation is indeed present. For instance, Taylor & Risk (1974) relied on noon-time observations from the mid-latitude ISR in Malvern (52.1°N, 2.3°W); also McDonald and Williams (1980) based their analysis on observations collected at the Malvern ISR selecting daytime conditions; Bilitza (1975) used noon-time observations but for the mid-latitude ISR located in Millstone Hill (42.6°N, 71.5°W); Brace and Theis (1978) results were based on LP observations from the Atmosphere Explorer C satellite between ± 50° of geographic latitude and for daytime conditions (solar zenith angles less than 85°). Then, it is not surprising that these authors found a remarkable anti-correlation. However, in the following years, the cumulated observations obtained by low-Earth-orbit (LEO) satellites carrying on board LPs and RPAs, both capable of obtaining in-situ observations of both N_e and T_e with a global coverage and for different local times (LTs), made it clear how the

suggested anti-correlation was not valid wherever and whenever (Brace & Theis, 1981; Brace et al., 1982). This evidence laid the foundations for the development of empirical T_e models based on T_e observations by LEO satellites or ISRs (Brace & Theis, 1981; Spenner & Plugge, 1979; Truhlik et al., 2012).

Although the anti-correlation was initially forsaken for modeling purposes, the interest in studying the correlation between N_e and T_e in the ionosphere kept its importance because it sheds light on the physical and dynamical properties of the ionospheric plasma. Indeed, plasma densities and temperatures significantly affect the plasma distribution function, and both concur to the energetic balance of the ionospheric plasma (Banks, 1969; Schunk & Nagy, 1978, 2009). As a consequence, ionospheric N_e and T_e are physical variables related to each other, whose correlation (if any) could help in distinguishing and identifying the physical phenomena affecting the energy budget of the ionosphere, as well as helping to model both N_e and T_e.

Over the years, the ever-growing number of in-situ N_e and T_e observations from LEO satellites, along with the long time series observations available from ISRs, allowed identifying patterns different from the common anti-correlation found in the first studies that were mostly focused on daytime and mid latitudes. Bailey et al. (2000), by analyzing Hinotori satellite in-situ observations at an altitude of 600 km for low latitudes and high solar activity conditions, observed a distinct difference in the relationship between N_e and T_e for daytime and nighttime hours. During daytime they observed the usual anti-correlation, while during nighttime T_e showed a positive correlation with N_e. Moreover, a positive correlation was also observed during daytime at magnetic latitudes lower than 10° around the geomagnetic equator. Bhuyan et al. (2002) used SROSS C2 satellite in-situ observations at an altitude of about 500 km to study the N_e and T_e variations at equatorial and low latitudes for low solar activity conditions. They found a general anti-correlation during daytime hours, and a lack of correlation during nighttime hours, this pattern being consistent across different seasons. Zhang & Holt (2004) discussed the correlation properties by taking advantage of a wide data set of observations collected by the mid-latitude Millstone Hill ISR from 1976 to 2001. Using ISRs vertical profiles, they were able to highlight the correlation properties in a wide range of altitudes from 200 to 500 km, which allowed discriminating differences in the N_e and T_e mutual behavior as a function of altitude. At topside ionosphere altitudes, Zhang & Holt (2004) found that N_e and T_e show a distinct anti-correlation during daytime hours, except for the summer season, when no correlation is evident. During nighttime, irrespective of the season, no evident correlation was found. Zhang et al. (2004) studied the correlation properties through observations taken by the mid-latitude ISR at Saint Santin (44.6°N, 2.2°E) from 1966 to 1987. In the range of altitude between about 300 and 500 km, they found a very distinct LT variation in the correlation coefficients between N_e and T_e. During daytime hours, N_e and T_e are anti-correlated and the anti-correlation intensifies at higher altitudes. Differently, during nighttime hours N_e and T_e are slightly positively correlated. This diurnal pattern of the correlation properties is consistent across different seasons at Saint Santin; this highlights a seasonal difference compared to corresponding results found at Millstone Hill by Zhang & Holt (2004), concerning daytime summer conditions. Lei et al. (2007) deeply investigated the N_e and T_e mutual behavior using observations from the Millstone Hill ISR, for the years 1976–2002, the low-latitude Arecibo (18.3° N, 66.7° W) ISR, for the years 1966–2002, and simulated values calculated from the National Center for Atmospheric Research Thermosphere-Ionosphere-Electrodynamics General Circulation Model. They pointed out that the N_e and T_e mutual variations at the F2-layer peak altitude are critically dependent on the N_e magnitude and, in turn, on their different dependence on the solar activity. National Center for Atmospheric Research Thermosphere-onosphere-Electrodynamics General Circulation Model simulated N_e and T_e at Millstone Hill location and at F2-layer peak altitude exhibited a fairly complex dependence. Specifically, Lei et al. (2007) found that there exist two N_e thresholds for which the correlation properties drastically change. When N_e is below $5{\cdot}10^5$ el/cm^3 and above $1.1{\cdot}10^6$ el/cm^3, N_e and T_e are positively correlated with a similar dependence on the solar activity level, that is, both increase with increased solar activity; differently, in the N_e range between $5{\cdot}10^5$ el/cm^3 and $1.1{\cdot}10^6$ el/cm^3, N_e and T_e are negatively correlated because, in this range, T_e decreases as the solar activity increases. Differently, at Arecibo location they found that only one N_e threshold exists at about $8.5{\cdot}10^5$ el/cm^3. When N_e is lower than this threshold, N_e and T_e are negatively correlated; while above this threshold, N_e and T_e are positively correlated. Kakinami et al. (2011a) extensively investigated the correlation properties through Hinotori satellite in-situ observations at an altitude of about 600 km, for high solar activity level, and magnetic dip latitudes (Mlat) less than about ±40°. Like Lei et al. (2007), also Kakinami et al. (2011a) showed how the correlation properties are dependent on the N_e magnitude. They highlighted the well-known negative correlation during daytime for N_e values relatively low. However, when N_e daytime values exceed a threshold of about $1{\cdot}10^6$ el/cm^3 (which is dependent on magnetic latitude, LT, longitude, and season), the correlation turns positive. This behavior is

particularly visible between 11:00 and 15:00 LT and around the geomagnetic equator (|Mlat| < 10°), when N_e and T_e show the characteristic "U-shape". Conversely, during nighttime hours they found a positive correlation. Kakinami et al. (2011b, 2013) extended the study by including in-situ observations by the DEMETER Sun-synchronous satellite between 660 and 710 km of altitude. These studies confirmed the characteristic "U-shape" in the relation between N_e and T_e which was observed for different latitudes, longitudes, seasons, and solar flux levels; however, it was particularly evident around the geomagnetic equator and between 11:00 and 15:00 LT. Kakinami et al. (2011b) also investigated the spatial variations exhibited by N_e and T_e at Hinotori and DEMETER altitudes. They found that N_e and T_e are in general spatially anti-correlated, with T_e minima appearing at N_e maxima location, and vice-versa. However, besides the spatial anti-correlation, the values of corresponding maxima and minima are not always inversely correlated. Kakinami et al. (2011b) suggested that at low latitudes T_e does not completely correlate with in-situ N_e values and that the integrated N_e along the geomagnetic field line from ground to the satellite altitude would better correlate with T_e. DEMETER satellite in-situ observations were also used by Su et al. (2015) to investigate the correlation properties for the two LTs probed by the satellite, that is, at about 10:30 and 22:30 LT, between ±65° of geographic latitude, for the mid and low solar activity years between 2006 and 2009. Their extensive study confirmed the prominent negative correlation at low and mid latitudes in the daytime sector (around 10:30 LT), while the negative correlation weakens at higher latitudes. In the nighttime sector (around 22:30 LT) they found a positive correlation near the geomagnetic equator for low solar activity conditions, and a slightly negative correlation at mid latitudes, with significant seasonal variations. Yan et al. (2022) have recently performed a detailed analysis of the correlation in the topside ionosphere using different satellites: China Seismo-Electromagnetic Satellite (CSES-01), Swarm A and B, and Challenging Minisatellite Payload. Their study is confined to the hours around 14:00 LT, and to the magnetic latitudes within ±50°. They found a consistent negative correlation between N_e and T_e at 14:00 LT, for the four satellites involved in the study. In agreement with the Lei et al. (2007) and Kakinami et al. (2011a) findings, also Yan et al. (2022) found that the negative correlation is particularly evident for relatively low N_e values, while it weakens and eventually becomes positive when N_e exceeds a certain threshold. In addition, the correlation showed variations with season and magnetic latitude.

These studies have shown that the correlation properties in the ionosphere are critically dependent on the altitude, LT, latitude, season, N_e values, and solar activity due to the different response by N_e and T_e to the solar energy flux input. As a consequence, to appropriately describe the N_e and T_e mutual behavior, all of these dependencies have to be considered and described. The European Space Agency's (ESA) Swarm satellites mission (Friis-Christensen et al., 2006) offers the opportunity to improve the knowledge of the correlation properties using in-situ observations from LPs in the topside ionosphere between about 450 and 500 km of altitude. The Swarm satellites are in a circular near-polar orbit and thus they have accumulated a huge amount of in-situ observations covering different latitudes, LTs, seasons, and solar activity levels since their launch at the end of 2013. Our intention is to take advantage of this wealth of information to deeply investigate the correlation between N_e and T_e in the topside ionosphere. Past studies focused on low and mid latitudes covered by different LEO satellites and by the available ISRs, while high latitudes have never been investigated. Since Swarm satellites also cover the high latitudes, we aim to address this gap. Thus, using Swarm in-situ observations collected between 2014 and 2022, the correlation properties between N_e and T_e in the topside ionosphere are investigated on a global basis and as a function of LT and season. Furthermore, N_e and T_e observations collected by Arecibo, Jicamarca, and Millstone Hill ISRs in the last decades have been used to derive correlation coefficients at Swarm B altitude, which have been compared with those obtained with Swarm B observations.

The paper is organized as follows. Section 2 first describes the data sets used in this study with corresponding data filtering and sorting; after that, it describes the methodology used to calculate the Spearman rank correlation coefficient based on N_e and T_e in-situ observations. Section 3 collects and describes the results in the form of maps and time series, which are then discussed and interpreted in Section 4. The main conclusions are summarized in Section 5.

2. Data and Method

2.1. Swarm B Satellite Langmuir Probe Data

Swarm is a constellation composed of three LEO satellites launched by ESA at the end of 2013, and still operating. The Swarm mission focuses on the study of the geomagnetic field, electric currents in the magnetosphere and ionosphere, and the impact of the solar wind on the dynamics of the upper atmosphere on a global basis (Friis-Christensen et al., 2006). We focus on Swarm B flying in a circular near-polar orbit with an inclination of 87.75°

and an initial altitude of 510 km. Swarm B orbital configuration allows it to cover all the LTs within about 130–140 days. Swarm satellites are equipped with LPs which provide measurements of in-situ N_e and T_e along the satellite orbit, with a sampling frequency of 2 Hz in the harmonic mode (Catapano et al., 2022; Knudsen et al., 2017). In this study, we consider LP N_e and T_e observations collected by Swarm B from 1 January 2014 to 31 December 2022, baseline 05. In this timeframe, the Swarm B altitudinal variation has been relatively small, ranging between 500 and 525 km from ground. The Swarm data are freely downloadable at https://swarm-diss.eo.esa.int/. Only the standard product LP observations recorded mainly in high-gain mode were used and filtered using the flags provided with data (Swarm L1b Product Definition, 2018), as detailed by Pignalberi et al. (2021a) in their Section 2.1. Detailed information about Swarm data quality is available at https://swarm-diss.eo.esa.int/.

A brief discussion is necessary here about the functioning mode of the Swarm LPs, as one could argue that the results we are going to show are biased from the fact that both N_e and T_e come from the same instrument and the two measures could potentially influence each other. The most important point to highlight is that Swarm LPs, in their main functioning mode (i.e., the harmonic mode), do not perform the traditional sweep in voltage (V) for collecting ion and electron currents (Is), but rather work at fixed V points in which a periodic ripple is superimposed to the voltage baseline; this allows to infer also the local slope of the I-V curve, that is, the admittance. Through some mathematics, the Orbital Motion Limited theory (Fahleson, 1967; Mott-Smith & Langmuir, 1926) can be adapted to a combination of currents and admittances at the different sampling points, and N_e and T_e can be inferred; full details can be read in Knudsen et al. (2017). Indeed, for the Swarm LPs, it has been found that N_e measurements are more stable and reliable when obtained at the sampling point with negative V, that is, in the so-called "ion region" of a theoretical I-V curve (when a sufficiently negative voltage is applied to a LP only ions are collected). So, strictly speaking, in the standard product baseline 05, Swarm LPs actually provide the ion density, which can be considered nearly equivalent to an electron density recalling the well-known properties of a plasma (quasi-neutrality) and in the limits of the assumptions done in the calculation. T_e is instead inferred mainly from current and admittance in the so-called "retarded region" of a theoretical I-V curve, where the total potential sensed by the probe is still slightly negative but a significant electron current is still collected. In conclusion, the measure of N_e is completely independent of T_e, and, although ion current and admittance still enter in the calculation of T_e, the temperature trend is mainly driven by the variations of the retarded current and admittance.

2.2. Data Filtering and Sorting

In addition to the filtering based on LP's flags, we implemented other constraints. Specifically, only T_e observations in the range 100–6,000 K and N_e in the range 10^2–10^7 el/cm^3 were taken into account to filter out outliers. Since our analysis focuses on investigating the main features of the correlation between N_e and T_e, we considered only quiet-time periods for which the global geomagnetic index $Kp \leq 3$, to filter out observations collected during magnetically disturbed conditions. The reliability of Swarm T_e observations at large-scale was recently assessed by comparison with ISRs observations and IRI modeled values (Pignalberi et al., 2021a). However, Swarm T_e observations show also some rapid fluctuations and spikes, due to small-scale structures, at low and mid latitudes and at specific magnetic local times (MLTs) around 09 MLT and 15 MLT. Such features were evidenced by Pignalberi et al. (2021b) by calculating the *Rate Of change of electron TEmperature Index* (ROTEI) from Swarm T_e observations. To assess the possible impact of such T_e variations on the correlation coefficient calculation (described in Section 2.3), we first excluded T_e observations recorded at low and mid latitudes for which the corresponding ROTEI values exceeded a fixed threshold. We tried different ROTEI thresholds and repeated the calculation of correlation coefficients with selected T_e data sets. Since no clear difference in the values of correlation coefficients were found by using different ROTEI thresholds, we decided not to apply any filter based on ROTEI. This testifies the robustness of the statistical procedure for correlation coefficients calculation that will be described in Section 2.3.

Observations were then sorted to highlight the main spatial, diurnal, and seasonal variations of the correlation between N_e and T_e. The seasonal dependence has been characterized by selecting observations in three bins:

- June solstice: by selecting the months of May, June, July, and August, to represent the summer season in the Northern hemisphere and the winter season in the Southern one;
- December solstice: by selecting the months of November, December, January, and February, to represent the winter season in the Northern hemisphere and the summer season in the Southern one;

- Equinoxes: by selecting the months of March, April, September, and October, to represent the equinoctial seasons in both hemispheres. Since no evident differences among equinoxes were found from a preliminary analysis, we merged the two equinoxes in a single bin.

For each season, observations were sorted as a function of the Quasi-Dipole (QD) magnetic latitude (Laundal & Richmond, 2017) for the spatial characterization, and of the MLT for the diurnal characterization. Specifically:

- QD latitude: from −90° to 90° in steps of 1°, then 180 bins in total;
- MLT: from 00:00 (*hh*:*mm* where *hh* are hours and *mm* are minutes) to 24:00 in steps of 4 min, then 360 bins in total.

The extension of the Swarm B data set, 9 years, and the frequency sampling, 2 Hz, allowed for a high-resolution characterization of the spatial and diurnal variations on a global scale. Spatial and diurnal variations were represented in magnetic coordinates due to the strong coupling at Swarm altitudes between the ionospheric plasma dynamics and the geomagnetic field. In this study, we did not perform a longitudinal binning, even though longitudinal variations were actually observed in particular regions (e.g., in the Weddel Sea Anomaly, Liu et al., 2015).

2.3. Spearman Rank Correlation Coefficient Calculation

After binning, the original data set was sorted in 194,400 bins (3 seasons, 180 QD latitudes, 360 MLTs). For each of these bins, the correlation coefficient between N_e and T_e has been calculated. The number of N_e and T_e observations ranges between 1,000 and 3,000 for most of the bins.

Most of the previous investigations on the correlation between N_e and T_e relied on the calculation of the Pearson correlation coefficient, which is a statistical measure of the linear relation between two data sets of normally distributed variables. Thus, a linear dependence between N_e and T_e had to be assumed in those cases. However, this assumption does not properly represent the more complex dependence between N_e and T_e which is commonly observed in the ionosphere (Kakinami et al., 2011a; Lei et al., 2007). This is why we relaxed this assumption by calculating the Spearman rank correlation coefficient, which is a non-parametric measure of the monotonic relation between two data sets (Kendall & Stuart, 1973; Spearman, 1904; Zwillinger & Kokoska, 2000). In this case, no assumption is made on the statistical distributions of both data sets.

Spearman rank correlation coefficient (R_{Spearman}) is calculated by using the rank (R), in place of the actual observations, in the formula for the correlation coefficient calculation:

$$R_{\text{Spearman}} = \frac{\text{cov}(\text{R}(N_e),\text{R}(T_e))}{\sigma_{\text{R}(N_e)}\sigma_{\text{R}(T_e)}} \in [-1,1], \quad (1)$$

where cov is the covariance matrix and σ the variance.

R_{Spearman} varies between −1 and +1, where 0 implies no correlation, while −1 and +1 imply an exact decreasing and increasing monotonic relation between ranked variables, respectively. The monotonicity does not imply any specific functional variation, like the linear one in the Pearson correlation coefficient; then, if the two variables change together, but not necessarily at the same rate, the correlation between them will not be affected.

To calculate a value of the Spearman rank correlation coefficient according to Equation 1, the following statistical procedure has been applied to each bin:

1. Joint probability distributions (JPDs) between binned N_e and T_e observations are calculated. N_e (on *x*-axis) from 10^3 to 10^6 el/cm^3 is divided in 60 intervals (20 intervals for each order of magnitude) in logarithmic scale. T_e (on *y*-axis) from 0 to 6,000 K is divided in 60 intervals (intervals are 100 K wide) in linear scale;
2. For each N_e interval (on *x*-axis), the mean and standard deviation of T_e values conditioned by N_e are calculated. This is done by collecting all the T_e observations falling in a specific N_e interval, and then by calculating the corresponding mean and standard deviation of this T_e sub-dataset;
3. Equation 1 is applied to the mean T_e values conditioned by binned mean N_e values.

The procedure above described was applied to each of the 194,400 bins. An example is shown in Figure 1, that represents the bin for the equinoxes, MLT = [05:44; 05:48), and QD latitude = [0°; 1°); then, at the geomagnetic

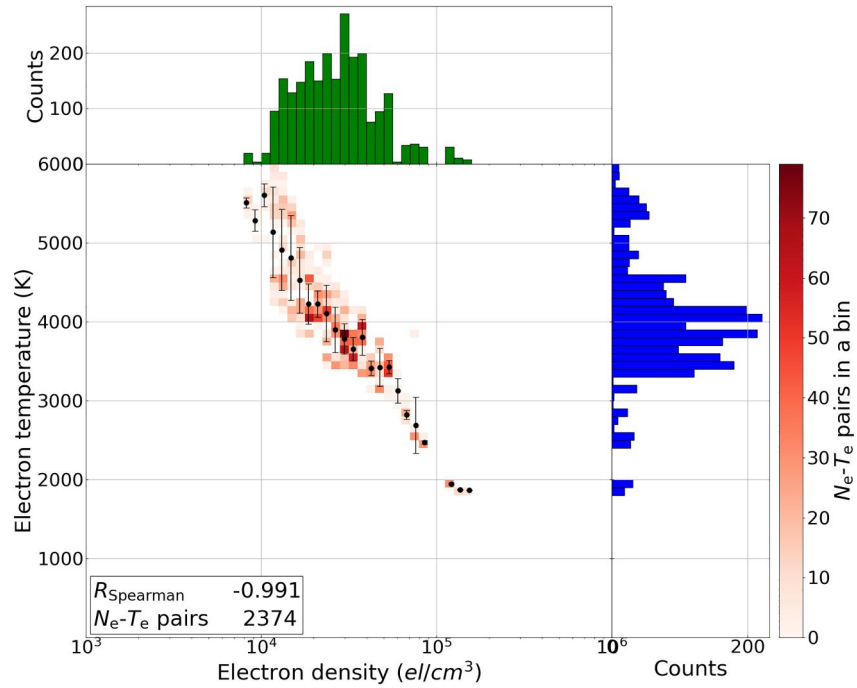

Figure 1. Joint probability distribution between N_e (x-axis) and T_e (y-axis) observations by Swarm B for the equinoxes, MLT = [05:44; 05:48), and Quasi-Dipole latitude = [0°; 1°). The number of pairs (N_e, T_e) of each bin is represented by a heat map; N_e and T_e statistical distributions are represented in green and blue, respectively. Mean and standard deviation of conditioned T_e values are represented as black points and error bars, respectively. The $R_{Spearman}$ value is shown in the bottom left legend, along with the number of total pairs (N_e, T_e).

equator during the morning overshoot hours. The mean and standard deviation of conditioned T_e values are represented as black points and error bars, respectively. The number of pairs (N_e, T_e) of each interval is represented in the scale of reds (heat map), while N_e and T_e statistical distributions are represented in green and blue, respectively. The corresponding $R_{Spearman}$ value is highlighted in the bottom left legend, along with the number of total pairs (N_e, T_e) in the JPD. This is a situation where the anti-correlation between N_e and T_e is well-known (Stolle et al., 2011; Yang et al., 2020), as testified by the value of $R_{Spearman} = -0.991$. This is also a case where the correlation is linear when representing N_e in logarithmic scale.

The remarkable anti-correlation shown in Figure 1 is just one of a wide range of possible dependencies. Figure 2 collects JPDs for four cases highlighting very different behaviors between N_e and T_e. Figure 2a represents the bin collecting data at the December solstice, MLT = [02:56; 03:00), and QD latitude = [40°; 41°), that is, during nighttime at mid latitudes. Under these conditions, N_e and T_e show a well-defined positive correlation although rather non-linear ($R_{Spearman} = 0.991$). Figure 2b represents the bin containing data for the December solstice, MLT = [04:04; 04:08), and QD latitude = [65°; 66°), that is, during nighttime at auroral latitudes. In this case, N_e and T_e are anti-correlated ($R_{Spearman} = -0.944$) but exhibiting a highly non-linear dependence compared to Figure 1. Besides positive and negative correlations, there are also cases where N_e and T_e show no correlation, as in Figures 2c and 2d. Figure 2c represents the bin containing data for the equinoxes, MLT = [11:32; 11:36), QD latitude = [−14°; −13°), that is, during daytime at the Southern crest of the equatorial ionization anomaly (EIA). Conversely, Figure 2d represents the bin containing data for the June solstice, MLT = [12:00; 12:04), QD latitude = [74°; 75°), that is, at noon in the polar cusp region. In both cases, N_e and T_e show no correlation ($R_{Spearman} = 0.005$ and 0.089, respectively), which is the manifestation of the lack of a definite relationship between N_e and T_e. The occurrence of a null or weak correlation between N_e and T_e depends upon the natural ionospheric variability for the selected conditions. In fact, we mitigated the dispersion of observations possibly associated with instrumental issues by filtering data using flags, discarding outliers, excluding data under geomagnetically disturbed conditions, and implementing the statistical procedure based on JPDs which is robust against scattered outliers. Moreover, the significance level of calculated $R_{Spearman}$ has been statistically verified

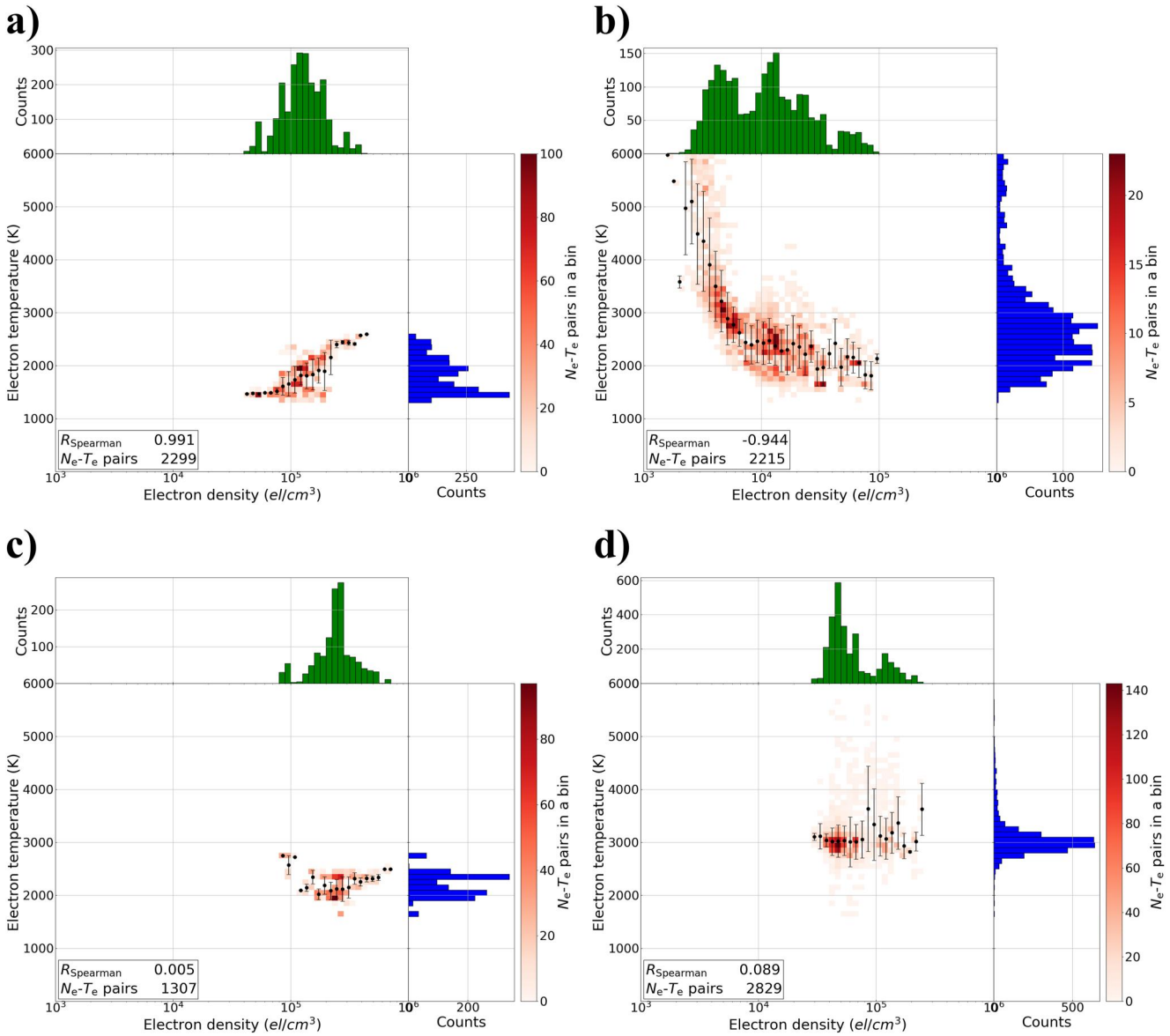

Figure 2. Joint probability distribution between N_e (x-axis) and T_e (y-axis) observations by Swarm B for the following cases: panel (a), December solstice, MLT = [02:56; 03:00), Quasi-Dipole (QD) latitude = [40°; 41°); panel (b), December solstice, MLT = [04:04; 04:08), QD latitude = [65°; 66°); panel (c), equinoxes, MLT = [11:32; 11:36), QD latitude = [−14°; −13°); panel (d), June solstice, MLT = [12:00; 12:04), QD latitude = [74°; 75°). In each panel, the number of pairs (N_e, T_e) of each bin is represented by a heat map; N_e and T_e statistical distributions are represented in green and blue, respectively. Mean and standard deviation of conditioned T_e values are represented as black points and error bars, respectively. The calculated $R_{Spearman}$ value is highlighted in the bottom left legend, along with the number of total pairs (N_e, T_e).

through a two-tailed hypothesis test at 5% of significance level. These statistical tests showed that also bins showing a null or weak correlation are statistically significant.

The occurrence of very different dependencies as a function of latitude, LT, and season, motivated us to analyze these characteristics in more detail to get a thorough picture.

2.4. Data From Incoherent Scatter Radars

ISRs utilize Thomson backscatter from ionospheric electrons to retrieve various ionospheric parameters, including N_e and T_e, in a range of altitude between about 100 and 1,000 km (Evans, 1969). N_e and T_e observations collected by Jicamarca (12.0°S, 76.8°W; QD latitude 0.2°N), Arecibo (18.2°N, 66.4°W; QD latitude 27.0°N), and

Millstone Hill (42.6°N, 71.5°W; QD latitude 51.8°N) ISRs, in the range of altitude 510 ± 30 km, have been used for comparison with Swarm B-derived results. The data set encompasses the years 1996–2020 for Jicamarca, 1974–2015 for Arecibo, and 1976–2020 for Millstone Hill. This is the same data set used by Pignalberi et al. (2021a) to validate Swarm satellites T_e observations from LPs. ISRs data were downloaded from the Madrigal database at http://cedar.openmadrigal.org.

Differently from Swarm B LP observations, ISRs observations are not continuous in time; however, the extension of the ISRs data set provided enough data to highlight the diurnal and seasonal variations of the correlation between N_e and T_e, albeit with a time resolution coarser than Swarm B. Specifically, N_e and T_e observations by ISRs were binned as a function of MLT in 30-min wide bins, while the seasonal binning is the same as the one described in Section 2.2. The number of ISRs observations in each bin ranges between 100 and 4,000, with the lowest number of observations for Jicamarca ISR and the highest for Millstone Hill ISR, as described by Figures 4–6 in Pignalberi et al. (2021a). For each of these bins, 144 in total (3 seasons, 48 MLTs) for each ISR, the methodology described in Section 2.3 has been applied to calculate corresponding $R_{Spearman}$ values. In the process, only the N_e and T_e observations by ISRs with a percentage error lower than 10% have been considered.

3. Results

3.1. Results From Swarm B Satellite

By applying the statistical procedure described in Section 2.3, values of $R_{Spearman}$ were calculated for each of the 194,400 bins mentioned in Section 2.2. In Figure 3 we represent the calculated $R_{Spearman}$ values as planar maps that are a function of MLT and QD latitude, for each season. In this way, the diurnal, latitudinal, and seasonal variations can be readily appreciated. Since one of the main novelties of this work is the study of the correlation between N_e and T_e at high latitudes, Figures 4 and 5 represent $R_{Spearman}$ variations at QD latitudes above ±50° through a polar representation for the Northern and Southern hemispheres, respectively. In the same Figures, we also represent the mean values of N_e and T_e, binned as described in Section 2.2, to illustrate their main spatial and diurnal patterns to simplify the discussion of correlation variations. Since no solar activity constraint has been applied, N_e and T_e maps are representative of the wide range of solar activity levels of the years 2014–2022 (from the maximum to the minimum of the last solar cycle).

Figure 3 shows very specific diurnal patterns at low and mid latitudes in the range |QD lat.| ≤ 50°. At these latitudes, from about 05:00 to about 19:00 MLT the well-known anti-correlation during sunlit hours is clear, while during nighttime hours values are either not correlated or positively correlated. An exception to this low- and mid-latitude diurnal pattern is given by the not-correlated values around the geomagnetic equator from 09:00 to 19:00 MLT. A reduced correlation is also visible during daytime at mid latitudes in the December solstice. High latitudes are characterized by anti-correlated values with the exception of the summer season (June solstice for the Northern hemisphere, December solstice for the Southern one) where not-correlated values characterize a belt around ±75° of QD latitude; the same pattern characterizes the Northern hemisphere at equinoxes. This feature is also the main seasonal variation exhibited by the correlation between N_e and T_e. Small patterns of positively correlated values are also visible around noon at the same high latitudes during summer.

As highlighted by most of the studies mentioned in the Introduction, the anti-correlation is an outstanding feature of the relation between N_e and T_e at daytime and mid latitudes, during the sunrise hours at low latitudes, and around ±60° of QD latitude during nighttime; while positive correlation is limited to nighttime hours at mid and low latitudes. The maps of N_e and T_e mean values help in the description and understanding of correlation main patterns, especially where marked increases of T_e are associated with marked decreases in N_e, and vice-versa. We remark here that N_e and T_e maps of Figures 3–5 give only an insight on the corresponding mean variations; for a deeper understanding, JPDs as those of Figures 1 and 2 should be individually considered. The peak of T_e around the geomagnetic equator at 06:00 MLT (also known as the morning overshoot, e.g., Stolle et al., 2011), along with the corresponding local minimum in N_e, account for the well-marked anti-correlation (as evidenced by Figure 1). Similarly, around ±60° of QD latitude during nighttime, where high T_e values are associated with corresponding low N_e values. However, this simplistic reasoning does not apply for example, at low latitudes from 09:00 MLT onwards, where high N_e are associated with low T_e values but with a poor correlation; the same during nighttime at mid and low latitudes. Detailed discussion of these features will be provided in Section 4.

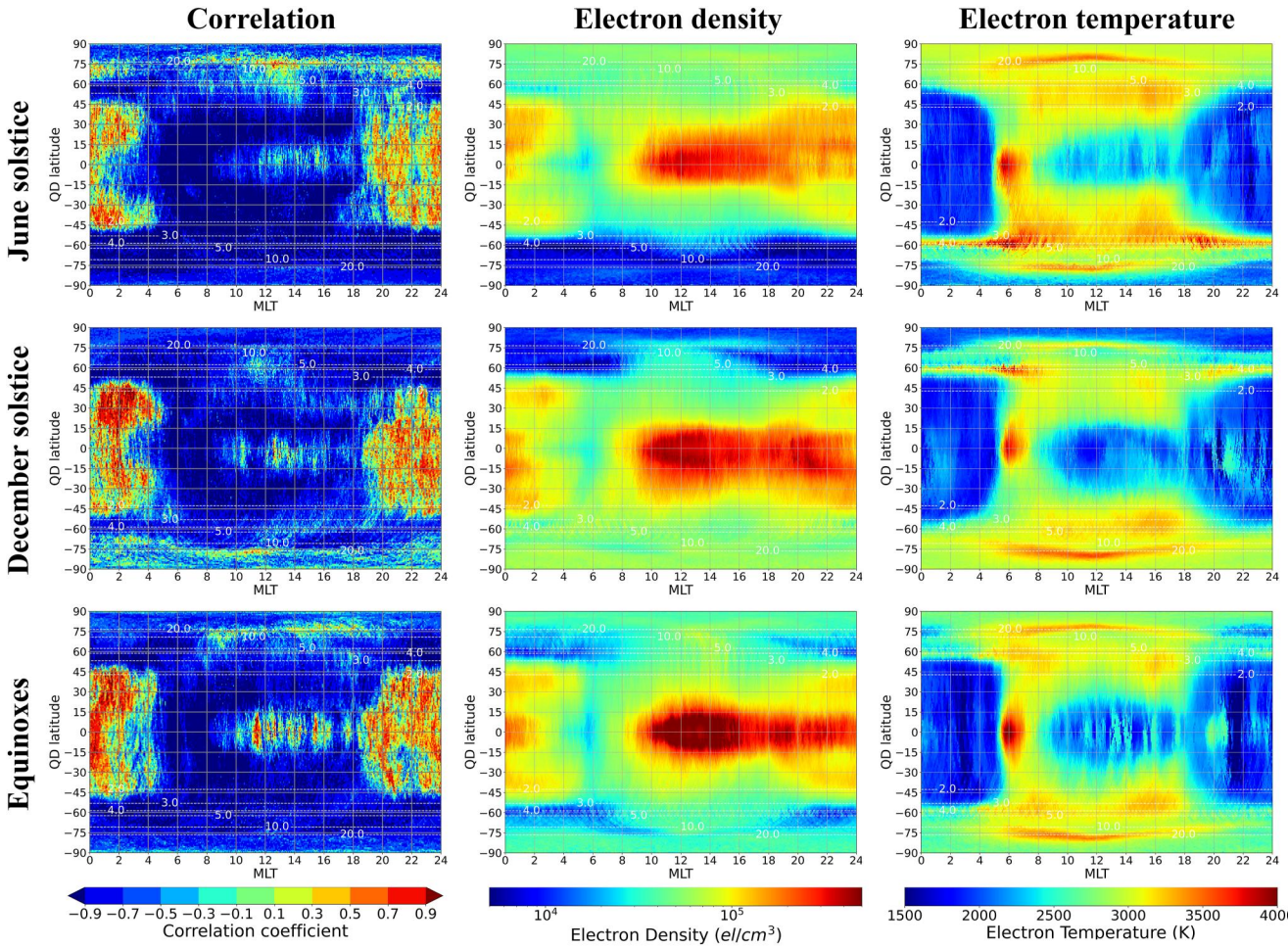

Figure 3. Global maps of R_{Spearman} correlation coefficient values (first column), electron density mean values (second column), and electron temperature mean values (third column), obtained using observations collected by Swarm B in the period 2014–2022. First row refers to the June solstice, second row refers to the December solstice, third row refers to the equinoxes. All maps are in MLT (*x*-axis) versus Quasi-Dipole latitude (*y*-axis) coordinates. The overlaid white dashed lines correspond to the L-shell values (2.0, 3.0, 5.0, 10.0, and 20.0) at 500 km of altitude.

To better describe the diurnal pattern of R_{Spearman} for different latitudinal ranges, mean zonal R_{Spearman} values have been calculated, based on the R_{Spearman} values reported in Figure 3. The latitudinal ranges have been chosen as follows: from 70°N to 80°N, from 70°S to 80°S, from 55°N to 65°N, from 55°S to 65°S, from 40° N to 50°N, from 40°S to 50°S, from 10°N to 20°N, from 10°S to 20°S, and from 5°S to 5°N. These latitudinal sectors are representative of the polar cusps, auroral boundaries, mid latitudes, EIA, and equatorial regions. Then, mean R_{Spearman} values have been calculated for each latitudinal sector as a function of MLT and for each season. Figure 6 shows the calculated mean zonal R_{Spearman} values. It is worth noting that Figure 6 plots provide an easier way to understand depiction of R_{Spearman} diurnal patterns compared to Figures 3–5, at the cost of smoothing out the corresponding latitudinal variations through the zonal averaging procedure.

The latitudinal dependence of R_{Spearman} for different MLT ranges has been revealed by calculating mean R_{Spearman} values for selected diurnal sectors, based on the R_{Spearman} values reported in Figure 3. Specifically, R_{Spearman} values were calculated in the following MLT ranges: from 01:00 to 03:00 MLT, from 05:00 to 07:00 MLT, from 11:00 to 13:00 MLT, and from 19:00 to 21:00 MLT. These diurnal sectors represent nighttime, sunrise, noon, and sunset conditions. For each diurnal sector, R_{Spearman} mean values have been calculated as a function of QD latitude and for each season. Figure 7 shows the corresponding results. It is worth noting that Figure 7 plots provide an easier way to understand depiction of R_{Spearman} latitudinal patterns compared to Figures 3–5, at the cost of smoothing out the corresponding MLT variations through the MLT averaging procedure.

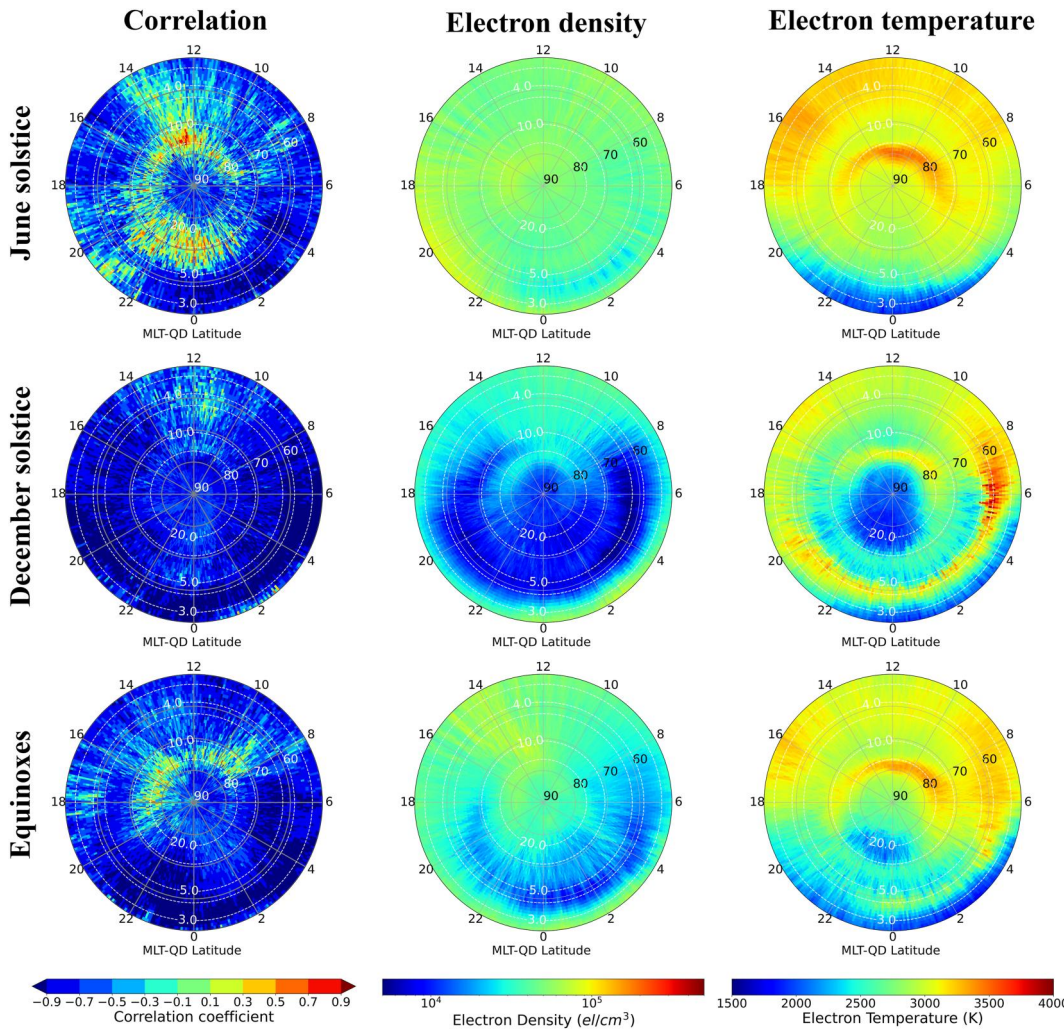

Figure 4. Maps of R_{Spearman} correlation coefficient values (first column), electron density mean values (second column), and electron temperature mean values (third column), in the Northern hemisphere obtained using observations collected by Swarm B in the period 2014–2022. First row refers to the June solstice, second row refers to the December solstice, third row refers to the equinoxes. All the polar maps are in MLT versus Quasi-Dipole latitude (from 50° to 90°) and refer to the Northern hemisphere. The overlaid white dashed lines correspond to the L-shell values (3.0, 5.0, 10.0, and 20.0) at 500 km altitude.

3.2. A Comparison With Incoherent Scatter Radars

This section describes a comparison between R_{Spearman} values obtained from Swarm B and those obtained from the equatorial ISR at Jicamarca, the low-/mid-latitude ISR at Arecibo, and the mid-latitude/subauroral ISR at Millstone Hill.

R_{Spearman} values for the three ISRs were calculated as explained in Section 2.4. Figure 8 summarizes the results of this comparison as a function of MLT, for the three seasons; black points represent R_{Spearman} values from ISRs observations, while blue lines are corresponding values from Swarm B observations at the QD latitude of the ISRs.

In general, the comparison shows a good qualitative agreement. At the equatorial latitudes (Jicamarca ISR) there is a general nighttime positive correlation between N_e and T_e. In morning hours, both Jicamarca ISR and Swarm B exhibit a strong anti-correlation between N_e and T_e; however, values are dependent on season. During daytime, the Swarm B data show rather negative correlation between N_e and T_e, while the ISR data show a rather positive correlation. This tendency of Swarm B data to differ from Jicamarca ISR may be due to a possible overestimation of T_e by Swarm, which is particularly significant at the equator, as shown in Figure 4 of Pignalberi et al. (2021a).

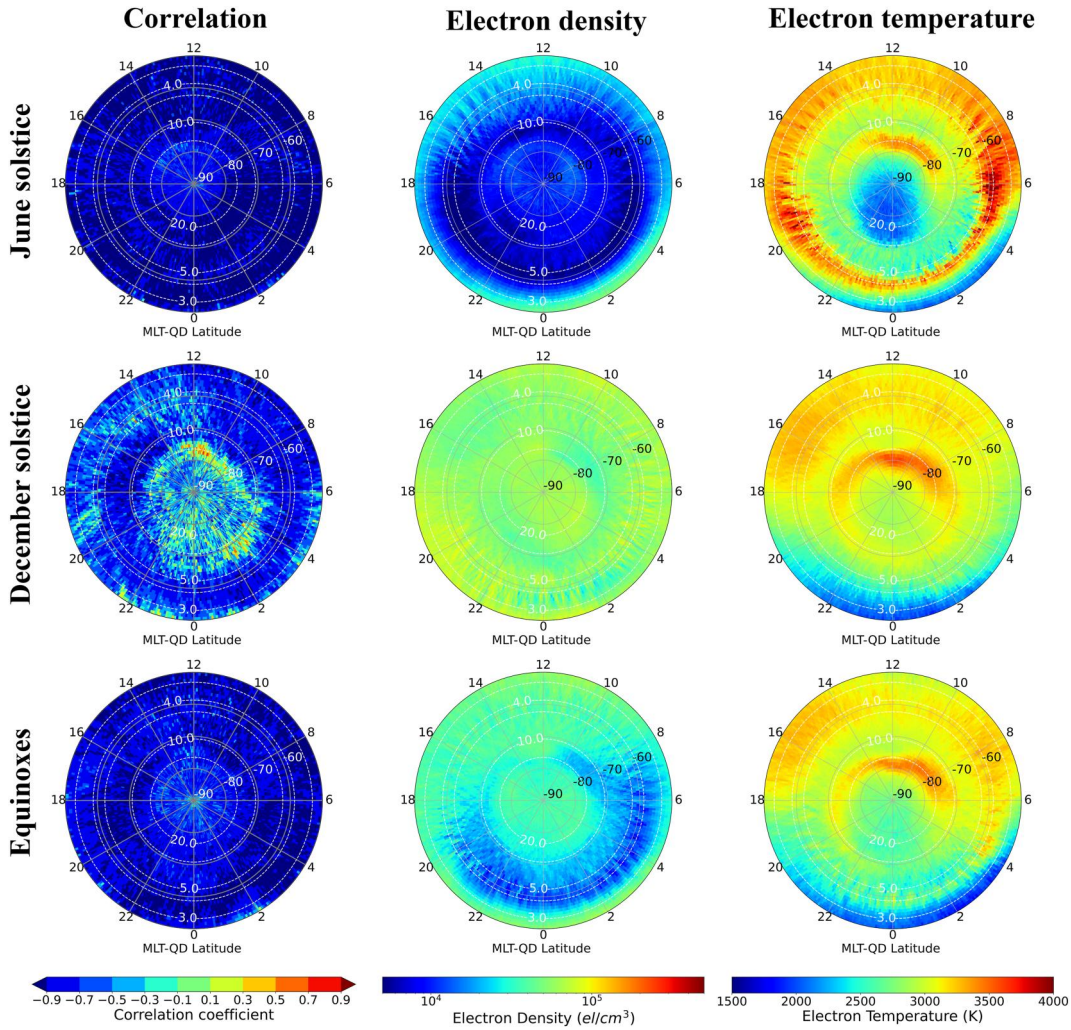

Figure 5. Maps of R_{Spearman} correlation coefficient values (first column), electron density mean values (second column), and electron temperature mean values (third column), in the Southern hemisphere obtained using observations collected by Swarm B in the period 2014–2022. First row refers to the June solstice, second row refers to the December solstice, third row refers to the equinoxes. All the polar maps are in MLT versus Quasi-Dipole latitude (from −50° to −90°) and refer to the Southern hemisphere. The overlaid white dashed lines correspond to the L-shell values (3.0, 5.0, 10.0, and 20.0) at 500 km altitude.

The comparison with Arecibo ISR shows remarkably good agreement for equinoxes, and still very good agreement for June solstice, when nighttime correlation is positive and daytime generally negative. This agrees with Pignalberi et al. (2021a) findings, which evidenced a better agreement between Swarm B and Arecibo ISR T_e observations compared to Jicamarca ISR observations. However, the comparison shows a significant difference for the winter solstice after sunrise when the ISR data exhibits a peak. The origin of this peak, if real, is not obvious and requires further investigation.

At Millstone Hill there is a good agreement between Swarm B and the ISR for daytime, especially for equinoxes and December solstice showing a negative correlation between N_e and T_e; while, at the June solstice, ISR data show no-correlation to slightly anti-correlated values, in agreement with findings by Zhang & Holt (2004). However, nighttime values differ significantly, with ISR data showing a positive correlation, whereas Swarm B data show a negative correlation. This can be due to different reactions of both techniques on possible heat inputs as, for example, the ring current heating or particles precipitation, which are not negligible at those latitudes (e.g., Hoegy, 1971). Moreover, Millstone Hill is located at the edge between mid and subauroral latitudes, where the correlation properties at nighttime change abruptly (see for instance Figure 3). Since the longitudinal dependence

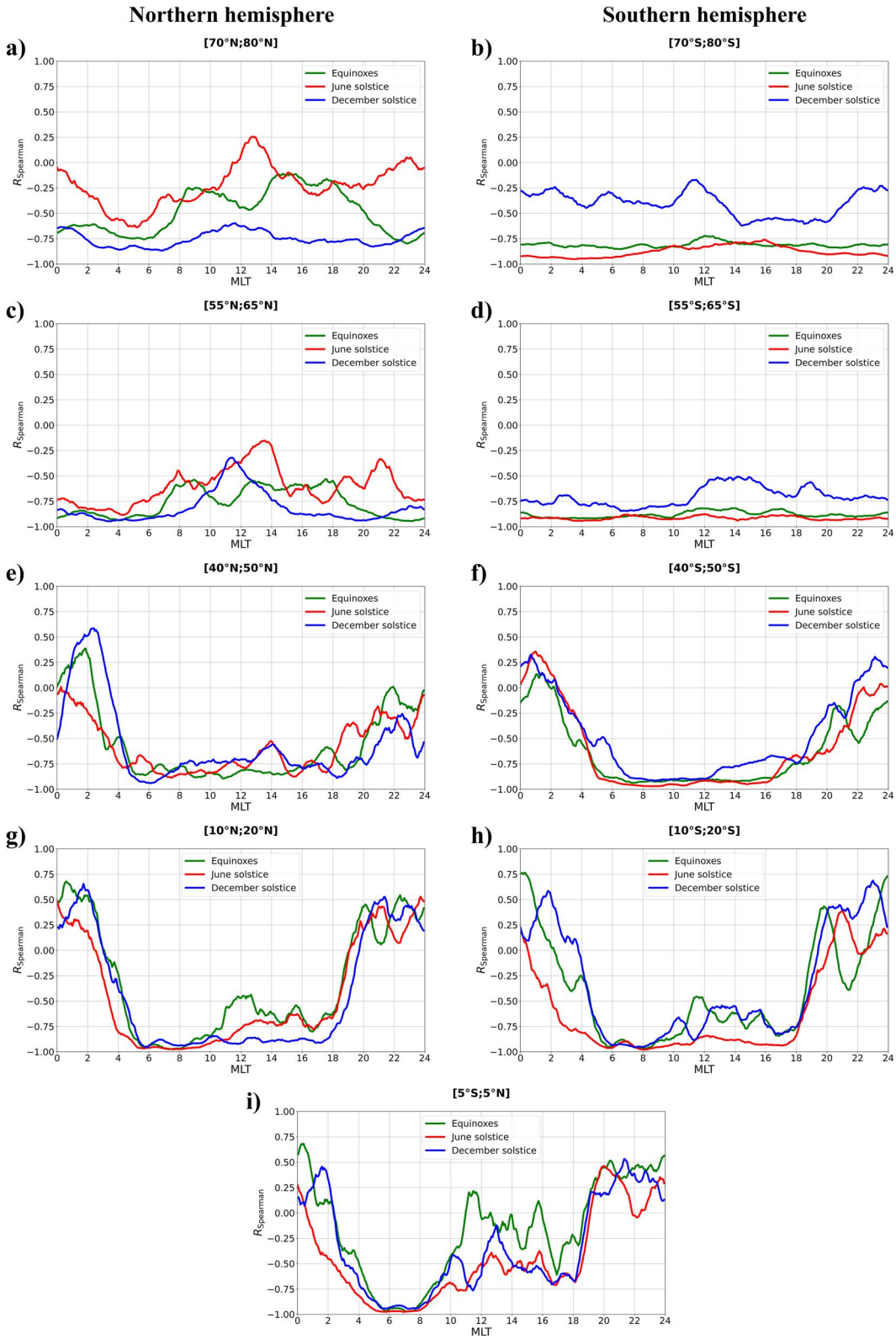

Figure 6.

has not been explicitly considered in the analysis of Swarm B data, the comparison at Millstone Hill location could be affected by local longitudinal variations not taken into account at this stage. Indeed, large longitudinal variations in the correlation were identified by Zhang & Holt (2004) and Zhang et al. (2004) by comparing results from observations collected by Millstone Hill and Saint Santin mid-latitude ISRs. Since ISRs data set encompasses past solar cycles, where the solar activity reached levels much higher than the data set covered by the Swarm mission, a solar activity dependence of the results cannot be excluded a-priori. This suggests that the observed differences need further investigation which are out of the scope of the present paper.

4. Discussion

Results shown in Figures 3–8 have highlighted how complex is the dependence between N_e and T_e in the topside ionosphere at an altitude of around 500 km. In fact, these two parameters are strictly related to each other in the electron energy conservation equation (Banks, 1969; Schunk & Nagy, 1978). Their variations depend upon three main physical processes: (a) the electron heating by photoelectrons, produced mainly by extreme ultraviolet (EUV) solar radiation and particles precipitation; (b) the electron cooling by heat transfer to ions and neutrals; (c) the heat flux due to thermal conduction and field-aligned currents. The interplay between these three physical processes describes the energy balance of the ionospheric plasma, and then the associated thermal properties. The electron heating by photoelectrons produces an increase in T_e whose rate is proportional to N_e (Schunk & Nagy, 1978). Differently, the electron cooling by heat transfer depends upon the altitude (Brace & Theis, 1978): in the lower ionosphere, below about 200 km, the electron cooling rate is mainly driven by collisions with neutrals and shows a dependence on N_e (Schunk & Nagy, 1978); in the upper ionosphere, the electron cooling rate is mainly driven by Coulomb collisions with ions and shows a dependence on N_e^2 (Schunk & Nagy, 1978). As a consequence, in absence of heat transport and below about 200 km, the heating and cooling rates are both proportional to N_e, so that N_e and T_e should be independent of each other. Instead, in the upper ionosphere, the cooling rate (which is proportional to N_e^2) overcomes the heating rate (which is proportional to N_e) and an inverse relation between N_e and T_e is expected, producing an anti-correlation between N_e and T_e.

This simplified thermal balance equilibrium describes fairly well the bottomside ionosphere below the F2-layer peak, where most of the photoelectrons are produced. However, in the topside ionosphere above the F2-layer peak, production and loss terms assume a lower importance and transport terms become relevant (Ratcliffe, 1972; Rishbeth & Garriott, 1969), so that the heat flux due to thermal conduction and field-aligned currents plays a relevant role. In the topside ionosphere, the electron conductivity parallel to the geomagnetic field lines dominates (Ratcliffe, 1972; Rishbeth & Garriott, 1969), which triggers a plasma motion and heat flux strictly along the geomagnetic field lines. The heat flux due to thermal conduction is dependent on the electron thermal conductivity K_e (Geisler & Bowhill, 1965), which is proportional to $T_e^{5/2}$ (Chapman & Cowling, 1958), and on the T_e gradient along geomagnetic field lines, that is, $\sin^2 I\, \mathrm{d}/\mathrm{d}h(K_e \mathrm{d}T_e/\mathrm{d}h)$ where I is the magnetic dip angle and h the vertical height. As a consequence, the heat flux due to thermal conduction maximizes at high latitudes where I is nearly $\pi/2$, and minimizes at low latitudes where geomagnetic field lines are nearly parallel to the Earth's surface.

It is then clear how the processes concurring to the electrons thermal balance in the ionosphere are strongly dependent on altitude, and no general considerations can be drawn without specifying the ionospheric region under consideration. This was clearly evidenced by Zhang & Holt (2004) and Zhang et al. (2004) that, using Millstone Hill and Saint Santin ISRs observations between 200 and 500 km, showed that the correlation between N_e and T_e is strongly dependent on altitude. Since our study concerns the topside ionosphere, the heat flux, that is, the transport of energy along geomagnetic field lines, assumes a relevant role in the description of the correlation between N_e and T_e. This is particularly evidenced by R_{Spearman} values at nighttime and at QD latitude $\sim |50°|$ (see for instance Figure 3) where the correlation abruptly changes from positive (or no correlation) to negative in the transition from closed to open geomagnetic field lines, that is, from the inner to the outer plasmasphere (Brace

Figure 6. Mean values of R_{Spearman} (y-axis) as a function of MLT (x-axis), for the three seasons (equinoxes in green, June solstice in red, December solstice in blue), and for different Quasi-Dipole (QD) latitude ranges. Each panel represents a different zonal range in QD coordinates: panel (a) from 70°N to 80°N, panel (b) from 70°S to 80°S, panel (c) from 55°N to 65°N, panel (d) from 55°S to 65°S, panel (e) from 40°N to 50°N, panel (f) from 40°S to 50°S, panel (g) from 10°N to 20°N, panel (h) from 10°S to 20°S, and panel (i) from 5°S to 5°N.

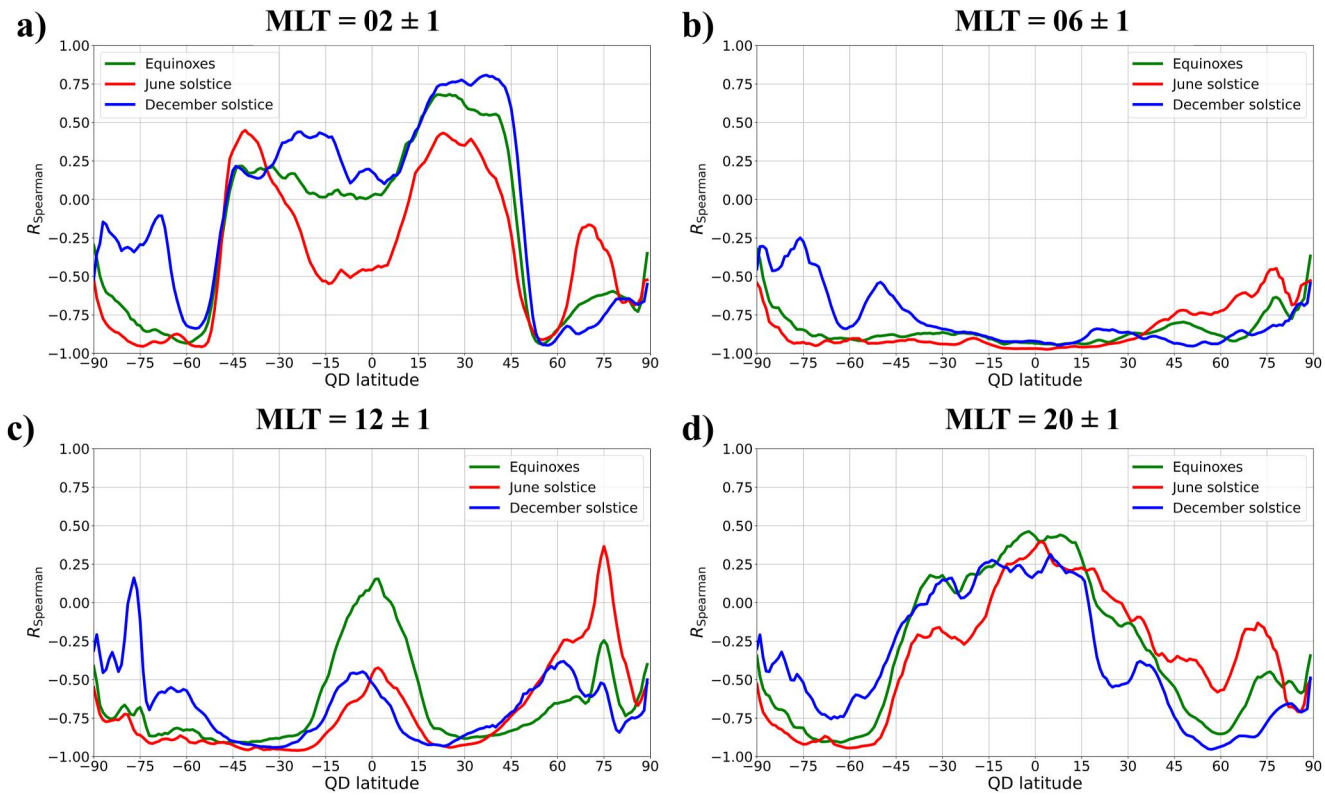

Figure 7. Mean values of $R_{Spearman}$ (y-axis) as a function of Quasi-Dipole latitude (x-axis), for the three seasons (equinoxes in green, June solstice in red, December solstice in blue), and for different MLT ranges. Each panel represents a different MLT sector: panel (a) from 01:00 to 03:00 MLT, panel (b) from 05:00 to 07:00 MLT, panel (c) from 11:00 to 13:00 MLT, and panel (d) from 19:00 to 21:00 MLT.

et al., 1982). At high latitudes, that is, at QD latitude $\gtrsim |50°|$, open geomagnetic field lines allow ionosphere-magnetosphere-solar wind coupling and very specific correlation features are identified, which are carefully described in Section 4.1. At mid latitudes, most of the well-known correlation features have been found and a corresponding discussion in the framework of existing studies is provided in Section 4.2. Section 4.3 focuses on low latitudes that deserve particular attention due to the specific correlation properties occurring during the development of the EIA.

4.1. High Latitudes

At high latitudes, an anti-correlation between N_e and T_e has been found in correspondence with low values of N_e (Prolss, 2006). In particular, Lei et al. (2007), Kakinami et al. (2011a) and subsequent works have pointed out that this anti-correlation emerges for N_e values between $5{\cdot}10^5$ and 10^6 el/cm^3. Apart from the specific values of eventual thresholds, our findings are consistent with this behavior. In fact, an anti-correlation can be statistically observed in those regions where N_e is very low and assumes local minima values, as we can see in Figures 4 and 5, and in Figures 6c and 6d. In particular, in both hemispheres a negative correlation is observed in correspondence with the lowest values of N_e, regardless of the season. These density minima occur especially at subauroral latitudes in the nightside, at the boundaries between the auroral oval and the main ionospheric trough, where plasma dynamics is dominated by particles precipitation associated mainly with processes occurring in the geomagnetic tail and the coupling with the plasmasphere. A possible explanation of the occurrence of such an anti-correlation co-located with low values of N_e is the consequent reduced collisional cooling. In fact, when N_e is low, the increased energy (and T_e) in the nightside ionosphere, associated with plasma energy and momentum exchange with the magnetosphere, is not effectively balanced by collisions. Thus, on one side the decrease of N_e corresponds to a decrease in thermal electron heat capacity; on the other side, the decrease of electron (and ion) density depletes the number of particles that can collide with the incoming ones (Wang et al., 2006) drastically

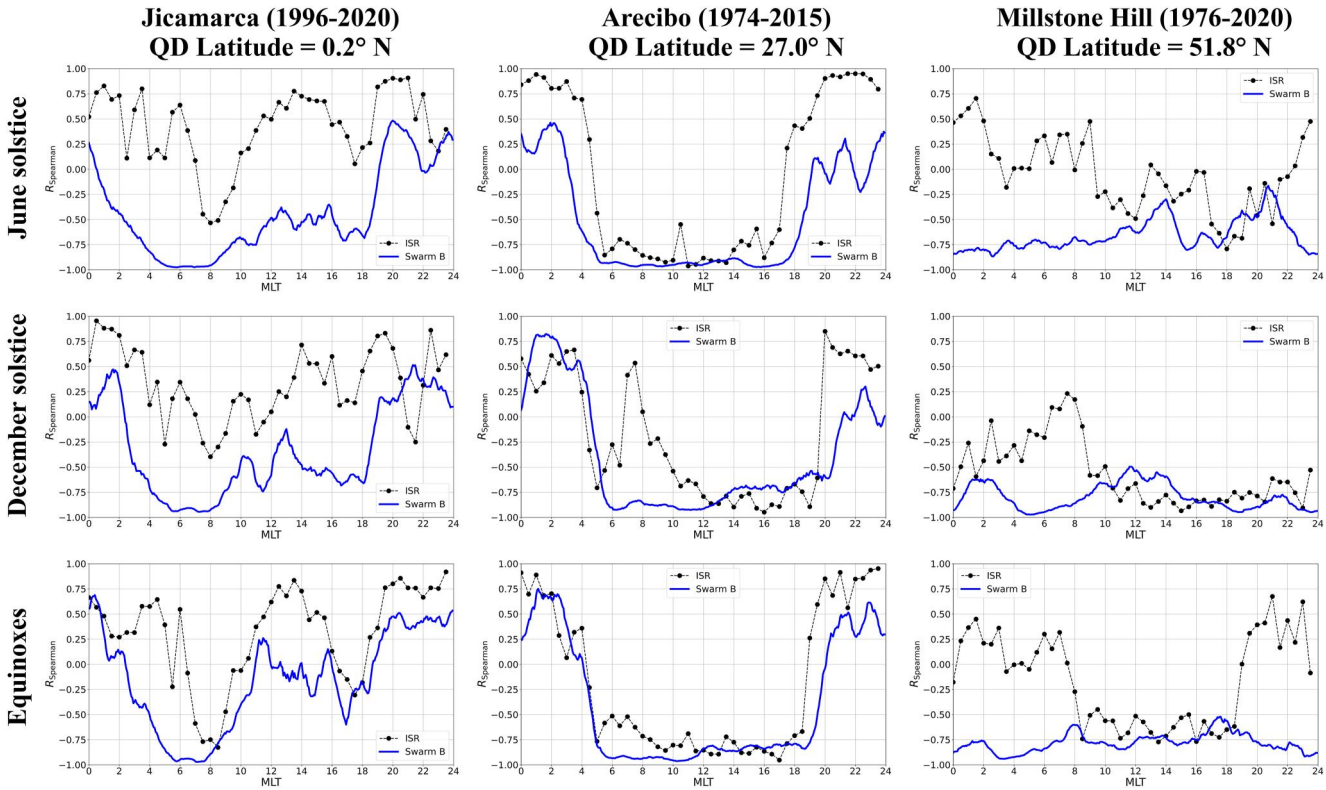

Figure 8. $R_{Spearman}$ values (y-axis) as a function of MLT (x-axis), for the Jicamarca (first column panels), Arecibo (second column panels), and Millstone Hill (third column panels) incoherent scatter radars (ISRs), at the altitudes of 510 ± 30 km. First row refers to the June solstice, second row refers to the December solstice, and third row refers to the equinoxes. In each panel, black points represent values calculated based on ISRs N_e and T_e observations, while blue lines are based on Swarm B N_e and T_e observations at the Quasi-Dipole latitude of the ISRs.

reducing, for example, ion-electron collision rate. This physical scenario is consistent with previous findings highlighting an anti-correlation for low values of N_e (Kakinami et al., 2011a; Lei et al., 2007).

Small patches of positive correlation can be observed at noon and very high QD latitudes (~80°) in both hemispheres during local summer (see Figures 6a and 7c). This may be associated with the precipitation of high energy plasma particles in the cusp. In fact, this region is characterized by a heavy precipitation of electrons due to the coupling between the open magnetosphere and the ionosphere in the dayside (Brinton et al., 1978; Foster, 1983; Milan et al., 2017; Prolss, 2006). The energy of precipitating electrons ranges between a few tens of eV to MeV, making the most energetic electrons a source of multiple ionizations in the upper atmosphere (Marif & Lilensten (2020) and references therein). The electrons created through collisions can in turn ionize other atoms or molecules. At the same time, the ionosphere quickly reacts to an increase in N_e redistributing the excess energy of incoming particles through an increased collision rate and the following reduction of energy of early precipitating particles. In fact, the increase in production of electrons is combined with the increase of ion concentration, which gives rise to an increased collisional cooling rate due to electron-ion collisions that causes a decrease in T_e. Thus, depending on the energy and pitch angle of precipitating (primary) electrons, the net effect may be an overall slight increase in electron density in correspondence of high values of electron temperature, which is a proxy of electron energy. This can generate a weak positive correlation between N_e and T_e in the dayside at cusp QD latitudes, as can be seen in the top-left panel of Figure 4, in the mid-left panel of Figure 5, and in Figures 6a and 7c. It is worth highlighting that, around noon, the density of particles precipitating within the cusp is more increased during summer than during winter (Christiansen et al., 2002; Fujii et al., 1981; Liou et al., 2001; Papitashvili et al., 2002; Wang et al., 2005). This may contribute to an increase of N_e in the cusp with a following increase of the correlation between N_e and T_e more accentuated in summer than in winter. Thus, particles precipitation seems to give rise to different dynamic regimes at cuspidal and auroral regions, being responsible for positive correlation

in the dayside (actually in the cusp region) and negative correlation in the nightside at auroral and subauroral regions, especially at latitudes where the main ionospheric trough is located (Karpachev, 2019).

The observed positive correlation close to the auroral boundary regions (70°–80° QD latitude), particularly evident in the Northern hemisphere during the June solstice (Figure 4), can be also related to the dynamics of the ionosphere-magnetosphere system. Indeed, the interplay between electron density and temperature influences the transfer of energy between the magnetosphere and the ionosphere linked to both the impulsive and convective dynamics of the geomagnetic tail region driven by solar wind changes (Akasofu, 1981; Alberti et al., 2017; Kamide & Kokubun, 1996). This can explain the observed positive correlation in the night-side sector due to the deposition of magnetospheric particles, mainly driven by the loading-unloading mechanism of the geomagnetic tail (L-shell > 10). Similarly, the positive correlation in correspondence of the polar cusp can be linked to the energy transfer from the solar wind to the high-latitude ionosphere as a result of the Joule heating, usually occurring poleward of the major particle heating region and especially in the morning sector and for L-shell ≤10 (Ahn et al., 1983). This is also confirmed in the Southern hemisphere by looking at the December solstice (Figure 5), although with a reduced value of the correlation, as well as a different spatial distribution, mainly centered across the dawn sector (Akasofu, 2021). However, we have to remark that the role of the ionosphere-magnetosphere coupling dynamics is particularly enhanced during active geomagnetic conditions, that is, when auroral substorms develop (Akasofu, 2021). Further investigations focused on specific case studies (i.e., during geomagnetic storms and/or magnetospheric substorms) or, in a statistical way, by selecting only periods with active geomagnetic conditions, are needed to properly characterize disturbed conditions.

High latitudes exhibit an inter-hemispheric asymmetry during equinoxes and daytime, showing no correlation in the Northern hemisphere while negative correlation in the Southern hemisphere. This is visible in Figures 3 and 7c for equinoxes, and by comparing Figures 6a and 6b for equinoxes. The inter-hemispheric asymmetry we find in the correlation between N_e and T_e is mainly associated to corresponding asymmetries in ionospheric plasma parameters. Laundal et al. (2017) associated inter-hemispheric asymmetries at high latitudes to the current offset between the magnetic and geographic poles. This introduces an asymmetry in the Sun illumination of high magnetic latitudes between the two hemispheres, which drives variations in the F-region plasma parameters. Similar conclusions were reached also by Pakhotin et al. (2021) who, through the study of the Poynting flux at 450 km of altitude, highlighted the existence of a hemispheric asymmetry in the input of electromagnetic energy from the Sun to the ionosphere.

4.2. Mid Latitudes

Mid latitudes are characterized by the well-known diurnal pattern showing a remarkable anti-correlation during sunlit hours, while a positive correlation (or no correlation) generally holds at nighttime (see Figures 3, 6, and 7). This is in agreement with previous studies based on the first LEO satellites and ISRs observations (Bilitza, 1975; Brace & Theis, 1978; McDonald & Williams, 1980; Taylor & Risk, 1974), and with more recent studies which take advantage of a better spatial and time coverage of observations (Bailey et al., 2000; Kakinami et al., 2011a, 2011b; Lei et al., 2007; Su et al., 2015; Yan et al., 2022; Zhang & Holt, 2004). The same diurnal pattern characterizes also the low latitudes except for the hours where the EIA develops. This testifies that the N_e and T_e mutual variations at mid and low latitudes, that is, where geomagnetic field lines are closed, are pretty similar. At mid latitudes, the diurnal pattern of the correlation is mainly described by the heat production-loss mechanisms associated with photoelectrons production-destruction mechanisms. At sunrise, the solar EUV radiation produces photoelectrons through photo-ionization of neutral constituents, thus increasing N_e. In a first stage, the N_e increase produces also a T_e increase because photoelectrons share their excess of energy with surrounding particles (the heating rate is proportional to N_e); however, proceeding with the N_e increase, more energy can be shared between photoelectrons and ions through Coulomb collisions, with a consequent cooling. Since the cooling term is proportional to N_e^2, cooling rapidly offsets the heating production, and produces the observed daytime anti-correlation between N_e and T_e. In this scenario, the N_e magnitude drives T_e variations, with different functional dependency as a function of N_e as highlighted by Lei et al. (2007). At sunset, the lack of solar EUV radiation stops the photoelectrons production with a consequent decrease of N_e and T_e, accounting for the positive correlation seen during nighttime (Figures 3, 6e, and 6f).

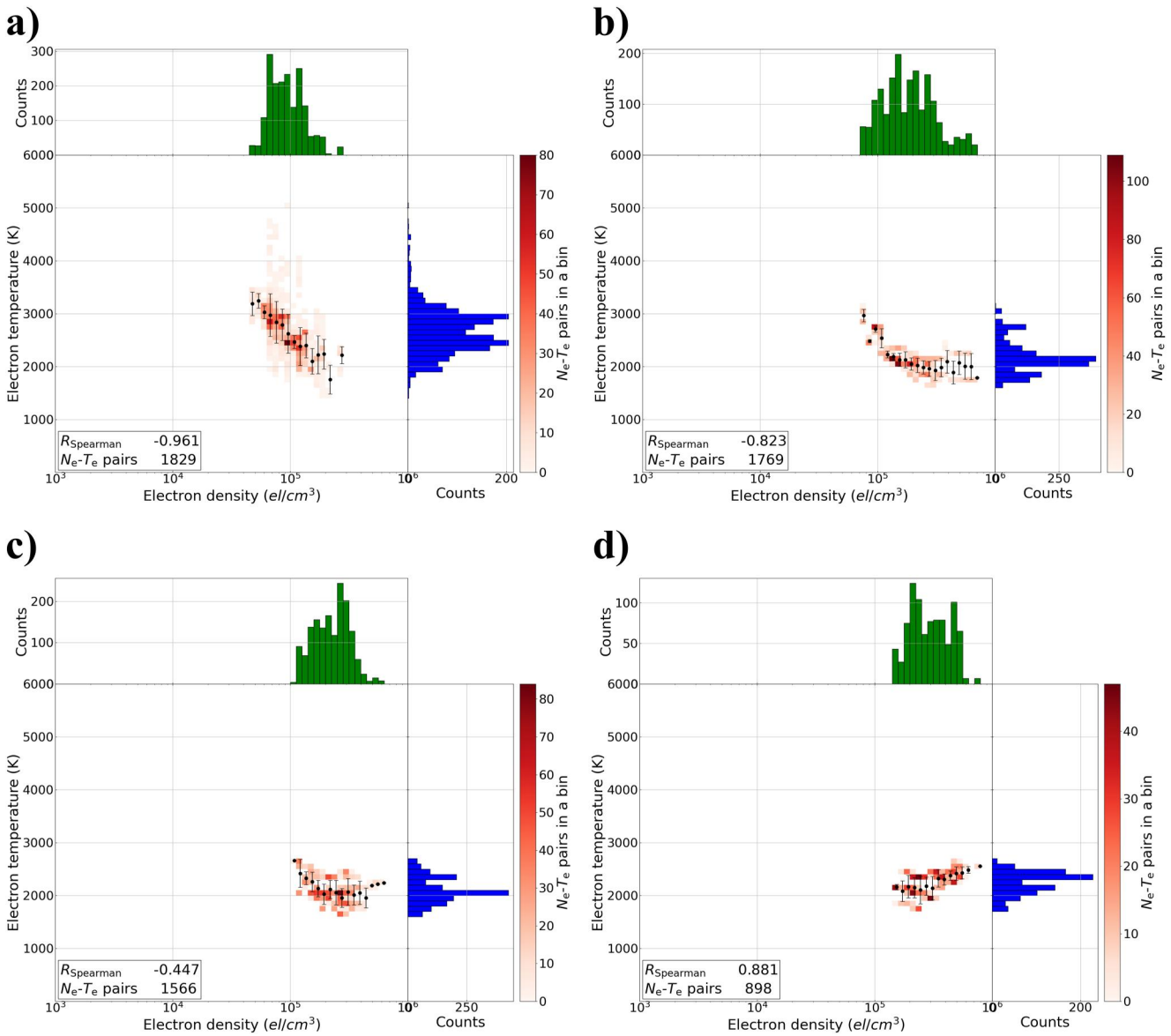

Figure 9. Joint probability distribution between N_e (x-axis) and T_e (y-axis) observations by Swarm B for the equinoxes, Quasi-Dipole latitude = [10°; 11°), for different MLTs: panel (a), MLT = [08:40; 08:44); panel (b), MLT = [10:16; 10:20); panel (c), MLT = [10:52; 10:56); panel (d), MLT = [11:24; 11:28). In each panel, the number of pairs (N_e, T_e) of each bin is represented by a heat map; N_e and T_e statistical distributions are represented in green and blue, respectively. Mean and standard deviation of conditioned T_e values are represented as black points and error bars, respectively. Calculated $R_{Spearman}$ value is highlighted in the bottom left legend, along with the number of total pairs (N_e, T_e).

4.3. Low Latitudes

Similarly to mid latitudes, low latitudes show a diurnal pattern characterized by an anti-correlation during sunlit hours and a positive correlation (or no correlation) at nighttime (see Figures 3, 6, and 7), except for the hours and latitudes characterized by the EIA development, that is, from about 09:00 MLT to sunset and for QD latitudes between about ±20°. Figure 6i shows the diurnal variation of the correlation at equatorial latitudes. At sunrise, there is an abrupt increase of T_e (see Figure 3), known as the equatorial morning overshoot; the T_e increase is very rapid due to the low values of N_e caused by the downward drift of plasma occurring in those conditions (Oyama et al., 1996), and to the more gradual increase of N_e compared to that of T_e (Stolle et al., 2011). That accounts for the clear anti-correlation seen for example, in Figure 1. This anti-correlation pattern holds for the first hours of the morning until the EIA starts developing. To better highlight this phenomenon, Figure 9 collects four JPDs at QD latitude = [10°; 11°), close to the

Northern crest of the EIA, for different MLTs between 08:40 and 11:28. Panel a) of Figure 9 shows that, before the EIA development, the usual anti-correlation between N_e and T_e holds for N_e values below $3 \cdot 10^5$ el/cm^3; panel b) of Figure 9 shows that the development of EIA increases N_e and causes a saturation of T_e at around 2,000 K; panel c) of Figure 9 shows the typical "U-shape" (Kakinami et al., 2011a, 2011b, 2013), where the dependence of T_e on N_e is strongly conditioned by the N_e value, with an anti-correlation below about $3 \cdot 10^5$ el/cm^3 and a positive correlation above this threshold; panel d) of Figure 9 shows that, with the full development of EIA, the correlation turns positive when the highest values of N_e are reached. This agrees with the results shown by Lei et al. (2007), who highlighted the same patterns through ISRs observations and simulation studies.

The daytime complex relationship between N_e and T_e is probably due to the fact that, for high values of N_e, there is also a concurrent increase in the neutral temperature (T_n), and hence in the ion temperature (T_i), the two temperatures being very close to each other. In these conditions, T_e is cooled due to the high values of N_e, but cannot drop below T_n (and T_i). Thus, from a certain level, T_e is forced to increase along with T_n (and T_i). Conversely, for very low values of N_e, T_n, and T_i are sufficiently low, so that T_e may decrease as N_e increases, until a specific value of N_e, after which it starts increasing (Kakinami et al., 2011a; Lei et al., 2007). At night, due to the thermodynamic equilibrium, T_n, T_e, and T_i are the same. As a consequence, an increase of N_e is followed by an increase of T_n, and hence N_e and T_e cannot be anti-correlated and are rather positively correlated.

5. Conclusions

In this work, we investigated the correlation between N_e and T_e in the topside ionosphere, at around 500 km of altitude, through in-situ observations collected by Swarm B satellite over 9 years. The extension of the data set and the satellite orbital configuration allowed studying the correlation properties for different latitudes, LTs, and seasons, with a detail never reached before. Spearman correlation coefficients have been calculated through a statistical analysis based on JPDs between N_e and T_e values collected for selected conditions, and mapped as a function of geomagnetic coordinates and seasons.

The performed analysis showed the following main features:

- High latitudes are characterized by a general pattern of negative correlation with the exception of the summer season where not-correlated to slightly positively correlated values characterize a belt around ±75° of QD latitude. This feature is also the main seasonal variation exhibited by the correlation between N_e and T_e. At these latitudes, diurnal variations are negligible. Small patches of positive correlation are present in the polar cusp around noon, while a clear negative correlation is evident at subauroral latitudes in the nightside, and at the boundary between the auroral oval and the main ionospheric trough. Correlation features have been discussed in the context of physical processes due to the coupling between the topside ionosphere and the overlying outer plasmasphere and magnetosphere, along open geomagnetic field lines;
- Mid latitudes are characterized by a well-defined diurnal pattern with the correlation showing remarkable negative values during sunlit hours and positive values at nighttime. This diurnal pattern holds in a wider range of QD latitudes, between ±50° of QD latitude, which is the region characterized by close geomagnetic field lines allowing a coupling between the topside ionosphere and the inner plasmasphere. Our findings confirm the results of previous studies;
- Low latitudes show a diurnal pattern similar to mid latitudes but with a significant difference for the hours and latitudes characterized by the EIA development. In that case, when very high N_e values are reached, the usual daytime negative correlation is lost; when N_e exceeds a certain threshold value, the correlation turns positive, possibly associated with the concurrent increase in the underlying neutral temperature, which is a lower limit for T_e. The full explanation of the mechanism leading to the "U-shape" in the correlation between N_e and T_e requires more in-depth studies;
- The comparison between correlation values obtained from Swarm B observations and corresponding ones from Arecibo, Jicamarca, and Millstone Hill ISRs showed a good qualitative agreement. The best agreement has been obtained for Arecibo, which is probably due to the higher power used by Arecibo ISR compared to that of Jicamarca and Millstone Hill ISRs. The comparison with Millstone Hill ISR highlighted significant differences possibly due to a longitudinal dependence that has not been explicitly considered in the analysis performed with Swarm B data.

Since we have filtered out Swarm B observations collected under disturbed geomagnetic conditions, this study represents a statistical climatological analysis of the correlation features between N_e and T_e. Future studies should focus on disturbed conditions. Moreover, possible longitudinal variations caused by known ionospheric asymmetries and large-scale anomalies need to be assessed for a thorough characterization of the complex behavior of N_e and T_e in the topside ionosphere. The explanation of the physical mechanisms leading to the "U-shape" in the EIA region requires more in-depth studies, possibly complementing satellites' observations with ISR measurements at different altitudes and/or physics-based models. By analyzing Swarm B LP observations at around 14 LT at low latitudes, Yan et al. (2022) highlighted the presence of two T_e branches from N_e versus T_e scatter plots. We verified that this phenomenology is limited to the LTs 13–15 and can affect the Spearman correlation coefficient calculation under these specific conditions. Further studies are needed to properly characterize this phenomenology and disclose if this is associated to an instrumental issue or to the natural ionospheric variability.

Results presented in this study are consistent with previous literature and can be of help for improving the characterization of the plasma behavior in the topside ionosphere, the description of the corresponding energy budget, and for a better understanding of the coupling mechanisms between the ionosphere, plasmasphere, and magnetosphere.

Data Availability Statement

European Space Agency Swarm data are publicly available via https://swarm-diss.eo.esa.int/. *Kp* geomagnetic activity index is available from OMNIWeb Data Explorer website (https://omniweb.gsfc.nasa.gov/form/dx1.html). Jicamarca, Arecibo, and Millstone Hill ISRs are available via the public access portal at http://cedar.openmadrigal.org.

Acknowledgments

Thanks to the European Space Agency for making Swarm data publicly available via https://swarm-diss.eo.esa.int/, and for the considerable efforts made for the LPs data calibration and maintenance. This publication uses data from Millstone Hill ISR made available via the public access portal at http://cedar.openmadrigal.org. The authors are indebted to the observatory directors and operators for the significant investments of their time, effort, expertise, and funds needed to acquire and provide measurement data to academic research over the years. Thanks to the two anonymous referees for their constructive comments and suggestions on the discussion and presentation of the results.

References

Ahn, B.-H., Akasofu, S.-I., & Kamide, Y. (1983). The Joule heat production rate and the particle injection rate as a function of the geomagnetic indices AE and AL. *Journal of Geophysical Research*, *88*(A8), 6275–6287. https://doi.org/10.1029/JA088iA08p06275

Akasofu, S.-I. (1981). Energy coupling between the solar wind and the magnetosphere. *Space Science Reviews*, *28*(2), 121–190. https://doi.org/10.1007/BF00218810

Akasofu, S.-I. (2021). A review of studies of geomagnetic storms and auroral/magnetospheric substorms based on the electric current approach. *Frontiers in Astronomy and Space Sciences*, *7*. https://doi.org/10.3389/fpas.2020.604750

Alberti, T., Consolini, G., Lepreti, F., Laurenza, M., Vecchio, A., & Carbone, V. (2017). Timescale separation in the solar wind-magnetosphere coupling during St. Patrick's Day storms in 2013 and 2015. *Journal of Geophysical Research: Space Physics*, *122*(4), 4266–4283. https://doi.org/10.1002/2016JA023175

Bailey, G. J., Su, Y. Z., & Oyama, K.-I. (2000). Yearly variations in the low-latitude topside ionosphere. *Annals of Geophysics*, *18*(7), 789–798. https://doi.org/10.1007/s00585-000-0789-0

Banks, P. M. (1969). The thermal structure of the ionosphere. *Proceedings of the IEEE*, *57*(3), 258–281. https://doi.org/10.1109/PROC.1969.6959

Bhuyan, P. K., Chamua, M., Subrahmanyam, P., & Garg, S. C. (2002). Diurnal, seasonal and latitudinal variations of electron temperature measured by the SROSS C2 satellite at 500 km altitude and comparison with the IRI. *Annals of Geophysics*, *20*(6), 807–815. https://doi.org/10.5194/angeo-20-807-2002

Bilitza, D. (1975). Models for the relationship between electron density and temperature in the upper ionosphere. *Journal of Atmospheric and Terrestrial Physics*, *37*(9), 1219–1222. https://doi.org/10.1016/0021-9169(75)90193-2

Bilitza, D. (1983). New descriptive temperature model. *Advances in Space Research*, *2*(10), 237–245. https://doi.org/10.1016/0273-1177(82)90398-2

Bilitza, D., Pezzopane, M., Truhlik, V., Altadill, D., Reinisch, B. W., & Pignalberi, A. (2022). The international reference ionosphere model: A review and description of an ionospheric benchmark. *Reviews of Geophysics*, *60*(4), e2022RG000792. https://doi.org/10.1029/2022RG000792

Brace, L. H., & Theis, R. F. (1978). An empirical model of the interrelationship of electron temperature and density in the daytime thermosphere at solar minimum. *Geophysical Research Letters*, *5*(4), 275–278. https://doi.org/10.1029/GL005i004p00275

Brace, L. H., & Theis, R. F. (1981). Global empirical models of ionospheric electron temperature in the upper F-region and plasmasphere based on in situ measurements from the atmosphere explorer-c, isis-1 and isis-2 satellites. *Journal of Atmospheric and Terrestrial Physics*, *43*(12), 1317–1343. https://doi.org/10.1016/0021-9169(81)90157-4

Brace, L. H., Theis, R. F., & Hoegy, W. R. (1982). A global view of F-region electron density and temperature at solar maximum. *Geophysical Research Letters*, *9*, 989–992. https://doi.org/10.1029/GL009i009p00989

Brinton, H. C., Grebowsky, J. M., & Brace, L. H. (1978). The high-latitude winter F region at 300 km: Thermal plasma observations from AE-C. *Journal of Geophysical Research*, *83*(A10), 4767–4776. https://doi.org/10.1029/JA083iA10p04767

Catapano, F., Buchert, S., Qamili, E., Nilsson, T., Bouffard, J., Siemes, C., et al. (2022). Swarm Langmuir probes' data quality validation and future improvements. *Geoscientific Instrumentation, Methods and Data Systems*, *11*(1), 149–162. https://doi.org/10.5194/gi-11-149-2022

Chapman, S., & Cowling, T. G. (1958). *The mathematical theory of non-uniform gases*. Cambridge University Press.

Christiansen, F., Papitashvili, V. O., & Neubert, T. (2002). Seasonal variations of high-latitude field-aligned currents inferred from Oersted and Magsat observations. *Journal of Geophysical Research*, *107*(A2). SMP 5-1–SMP 5-13. https://doi.org/10.1029/2001JA900104

Evans, J. (1969). Theory and practice of ionosphere study by Thomson scatter radar. *Proceedings of the IEEE*, *57*(4), 496–530. https://doi.org/10.1109/PROC.1969.7005

Fahleson, U. (1967). Theory of electric field measurements conducted in the magnetosphere with electric probes. *Space Science Reviews*, *7*(2–3), 238–262. https://doi.org/10.1007/BF00215600

Foster, J. C. (1983). An empirical electric field model derived from Chatanika radar data. *Journal of Geophysical Research*, *88*(A2), 981–987. https://doi.org/10.1029/JA088iA02p00981

Friis-Christensen, E., Lühr, H., & Hulot, G. (2006). Swarm: A constellation to study the Earth's magnetic field. *Earth Planets and Space*, *58*(4), 351–358. https://doi.org/10.1186/BF03351933

Fujii, R., Iijima, T., Potemra, T. A., & Sugiura, M. (1981). Seasonal dependence of large-scale Birkeland currents. *Geophysical Research Letters*, *8*(10), 1103–1106. https://doi.org/10.1029/GL008i010p01103

Geisler, J. E., & Bowhill, S. A. (1965). Ionospheric temperatures at sunspot minimum. *Journal of Atmospheric and Terrestrial Physics*, *27*(4), 457–474. https://doi.org/10.1016/0021-9169(65)90011-5

Hoegy, W. R. (1971). Probe and radar electron temperatures in an isotropic nonequilibrium plasma. *Journal of Geophysical Research*, *76*(34), 8333–8340. https://doi.org/10.1029/JA076i034p08333

Hunsucker, R. D. (1991). *Radio techniques for probing the terrestrial ionosphere*. Springer Berlin. https://doi.org/10.1007/978-3-642-76257-4

Jones, W. B., & Gallet, R. M. (1962). Representation of diurnal and geographical variations of ionospheric data by numerical methods. *Telecommunication Journal*, *29*, 129–149. Retrieved from https://nvlpubs.nist.gov/nistpubs/jres/66D/jresv66Dn4p419_A1b.pdf

Jones, W. B., & Gallet, R. M. (1965). Representation of diurnal and geographic variations of ionospheric data by numerical methods, II. Control of instability. *Telecommunication Journal*, *32*, 18–28.

Kakinami, Y., Kamogawa, M., Onishi, T., Mochizuki, K., Lebreton, J. P., Watanabe, S., et al. (2013). Validation of electron density and temperature observed by DEMETER. *Advances in Space Research*, *52*(7), 1267–1273. https://doi.org/10.1016/j.asr.2013.07.003

Kakinami, Y., Lin, C. H., Liu, J. Y., Kamogawa, M., Watanabe, S., & Parrot, M. (2011b). Daytime longitudinal structures of electron density and temperature in the topside ionosphere observed by the Hinotori and DEMETER satellites. *Journal of Geophysical Research*, *116*(A5), A05316. https://doi.org/10.1029/2010JA015632

Kakinami, Y., Watanabe, S., Liu, J. Y., & Balan, N. (2011a). Correlation between electron density and temperature in the topside ionosphere. *Journal of Geophysical Research*, *116*(A12), A12331. https://doi.org/10.1029/2011JA016905

Kamide, Y., & Kokubun, S. (1996). Two-component auroral electrojet: Importance for substorm studies. *Journal of Geophysical Research*, *101*(A6), 13027–13046. https://doi.org/10.1029/96JA00142

Karpachev, A. T. (2019). Variations in the winter troughs' position with local time, longitude, and solar activity in the Northern and Southern Hemispheres. *Journal of Geophysical Research: Space Physics*, *124*(10), 8039–8055. https://doi.org/10.1029/2019JA026631

Kendall, M. G., & Stuart, A. (1973). *The advanced theory of statistics, volume 2: Inference and relationship*. Griffin. Section 31.18.

Knudsen, D. J., Burchill, J. K., Buchert, S. C., Eriksson, A. I., Gill, R., Wahlund, J. E., et al. (2017). Thermal ion imagers and Langmuir probes in the Swarm electric field instruments. *Journal of Geophysical Research: Space Physics*, *122*(2), 2655–2673. https://doi.org/10.1002/2016JA022571

Laundal, K. M., Cnossen, I., Milan, S. E., Haaland, S. E., Coxon, J., Pedatella, N. M., et al. (2017). North–South asymmetries in Earth's magnetic field. *Space Science Reviews*, *206*(1–4), 225–257. https://doi.org/10.1007/s11214-016-0273-0

Laundal, K. M., & Richmond, A. D. (2017). Magnetic coordinate systems. *Space Science Reviews*, *206*(1–4), 27–59. https://doi.org/10.1007/s11214-016-0275-y

Lei, J., Roble, R. G., Wang, W., Emery, B. A., & Zhang, S. R. (2007). Electron temperature climatology at Millstone Hill and Arecibo. *Journal of Geophysical Research*, *112*(A2), A02302. https://doi.org/10.1029/2006JA012041

Liou, K., Newell, P. T., & Meng, C.-I. (2001). Seasonal effects on auroral particle acceleration and precipitation. *Journal of Geophysical Research*, *106*(A4), 5531–5542. https://doi.org/10.1029/1999JA000391

Liu, J. Y., Chang, F. Y., Oyama, K. I., Kakinami, Y., Yeh, H. C., Yeh, T. L., et al. (2015). Topside ionospheric electron temperature and density along the Weddell Sea latitude. *Journal of Geophysical Research: Space Physics*, *120*(1), 609–614. https://doi.org/10.1002/2014JA020227

Mahajan, K. K. (1977). Models of electron temperature in the ionospheric F-region using electron density height profiles. *Journal of Atmospheric and Terrestrial Physics*, *39*(5), 637–639. https://doi.org/10.1016/0021-9169(77)90075-7

Marif, H., & Lilensten, J. (2020). Suprathermal electron moments in the ionosphere. *Journal of Space Weather and Space Climate*, *10*, 22. https://doi.org/10.1051/swsc/2020021

McDonald, J. N., & Williams, P. J. S. (1980). The relationship between ionospheric temperature, electron density and solar activity. *Journal of Atmospheric and Terrestrial Physics*, *42*(1), 41–44. https://doi.org/10.1016/0021-9169(80)90121-X

Milan, S., Clausen, L., Coxon, J., Carter, J., Walach, M.-T., Laundal, K. M., et al. (2017). Overview of solar wind–magnetosphere–ionosphere–atmosphere coupling and the generation of magnetospheric currents. *Space Science Reviews*, *206*(1–4), 547–573. https://doi.org/10.1007/s11214-017-0333-0

Mott-Smith, H. M., & Langmuir, I. (1926). The theory of collectors in gaseous discharges. *Physical Review*, *28*(4), 727–763. https://doi.org/10.1103/PhysRev.28.727

Oyama, K.-I., Balan, N., Watanabe, S., Takahashi, T., Isoda, F., Bailey, G. J., & Oya, H. (1996). Morning overshoot of T_e enhanced by downward plasma drift in the equatorial topside ionosphere. *Journal of Geomagnetism and Geoelectricity*, *48*(7), 959–966. https://doi.org/10.5636/jgg.48.959

Pakhotin, I. P., Mann, I. R., Xie, K., Burchill, J. K., & Knudsen, D. J. (2021). Northern preference for terrestrial electromagnetic energy input from space weather. *Nature Communications*, *12*(1), 199. https://doi.org/10.1038/s41467-020-20450-3

Papitashvili, V. O., Christiansen, F., & Neubert, T. (2002). A new model of field-aligned currents derived from high-precision satellite magnetic field data. *Geophysical Research Letters*, *29*(14), 28-1–28-4. https://doi.org/10.1029/2001GL014207

Pignalberi, A., Coco, I., Giannattasio, F., Pezzopane, M., De Michelis, P., Consolini, G., & Tozzi, R. (2021b). A new ionospheric index to investigate electron temperature small-scale variations in the topside ionosphere. *Universe*, *7*(8), 290. https://doi.org/10.3390/universe7080290

Pignalberi, A., Giannattasio, F., Truhlik, V., Coco, I., Pezzopane, M., Consolini, G., et al. (2021a). On the electron temperature in the topside ionosphere as seen by Swarm satellites, incoherent scatter radars, and the international reference ionosphere model. *Remote Sensing*, *13*(20), 4077. https://doi.org/10.3390/rs13204077

Prolss, G. W. (2006). Subauroral electron temperature enhancement in the nighttime ionosphere. *Annals of Geophysics*, *24*(7), 1871–1885. https://doi.org/10.5194/angeo-24-1871-2006

Ratcliffe, J. A. (1972). *An introduction to the ionosphere and magnetosphere*. Cambridge University Press.

Rishbeth, H., & Garriott, O. (1969). Introduction to ionospheric physics. In *International geophysics series* (Vol. 14, pp. 126–159). Academic Press.

Schunk, R. W., & Nagy, A. F. (1978). Electron temperatures in the F region of the ionosphere: Theory and observations. *Reviews of Geophysics*, *16*(3), 355–399. https://doi.org/10.1029/RG016i003p00355

Schunk, R. W., & Nagy, A. F. (2009). *Ionospheres: Physics, plasma physics, and chemistry* (2nd ed.). Cambridge University Press.

Spearman, C. (1904). The proof and measurement of association between two things. *American Journal of Psychology*, *15*(1), 72–101. https://doi.org/10.2307/1412159.JSTOR1412159

Spenner, K., & Plugge, R. (1979). Empirical model of global electron temperature distribution between 300 and 700 km based on data from Aeros-A. *Journal of Geophysics*, *46*(1), 43–56. Retrieved from https://journal.geophysicsjournal.com/JofG/article/view/286

Stolle, C., Liu, H., Truhlík, V., Luhr, H., & Richards, P. G. (2011). Solar flux variation of the electron temperature morning overshoot in the equatorial F region. *Journal of Geophysical Research*, *116*(A4), A04308. https://doi.org/10.1029/2010JA016235

Su, F., Wang, W., Burns, A. G., Yue, X., & Zhu, F. (2015). The correlation between electron temperature and density in the topside ionosphere during 2006–2009. *Journal of Geophysical Research: Space Physics*, *120*(12), 10724–10739. https://doi.org/10.1002/2015JA021303

Swarm L1b Product Definition. (2018). *SW-RS-DSC-SY-0007*. National Space Institute, Technical University of Denmark. Retrieved from https://earth.esa.int/documents/10174/1514862/Swarm_L1b_Product_Definition

Taylor, G. N., & Risk, K. J. (1974). Empirical relationships between F-region electron density and temperature at Malvern. *Journal of Atmospheric and Terrestrial Physics*, *36*(8), 1427–1430. https://doi.org/10.1016/0021-9169(74)90220-7

Truhlik, V., Bilitza, D., & Triskova, L. (2012). A new global empirical model of the electron temperature with the inclusion of the solar activity variations for IRI. *Earth Planets and Space*, *64*(6), 531–543. https://doi.org/10.5047/eps.2011.10.016

Wang, H., Luhr, H., & Ma, S. Y. (2005). Solar zenith angle and merging electric field control of field-aligned currents: A statistical study of the Southern Hemisphere. *Journal of Geophysical Research*, *110*(A3), 306. https://doi.org/10.1029/2004JA010530

Wang, W., Burns, A. G., & Killeen, T. L. (2006). A numerical study of the response of ionospheric electron temperature to geomagnetic activity. *Journal of Geophysical Research*, *111*(A11), A11301. https://doi.org/10.1029/2006JA011698

Yan, R., Xiong, C., Zhima, Z., Shen, X., Liu, D., Liu, C., et al. (2022). Correlation between *Ne* and *Te* around 14:00 LT in the topside ionosphere observed by CSES, Swarm and CHAMP satellites. *Frontiers in Earth Science*, *10*, 860234. https://doi.org/10.3389/feart.2022.860234

Yang, T. Y., Park, J., Kwak, Y. S., Oyama, K. I., Minow, J. I., & Lee, J. J. (2020). Morning overshoot of electron temperature as observed by the Swarm constellation and the International Space Station. *Journal of Geophysical Research: Space Physics*, *125*(2), e2019JA027299. https://doi.org/10.1029/2019JA027299

Zhang, S. R., & Holt, J. M. (2004). Ionospheric plasma temperatures during 1976–2001 over Millstone Hill. *Advances in Space Research*, *33*(6), 963–969. https://doi.org/10.1016/j.asr.2003.07.012

Zhang, S. R., Holt, J. M., Zalucha, A. M., & Amory-Mazaudier, C. (2004). Midlatitude ionospheric plasma temperature climatology and empirical model based on Saint Santin incoherent scatter radar data from 1966 to 1987. *Journal of Geophysical Research*, *109*(A11), A11311. https://doi.org/10.1029/2004JA010709

Zwillinger, D., & Kokoska, S. (2000). *CRC standard probability and statistics tables and formulae*. Chapman & Hall. Section 14.7.